Determination of electric field distributions in superconductors via magneto-optical imaging and the Faraday law

Ch. Jooss and V. Born
Institut für Materialphysik, Friedrich Hund Platz 1, 37077 Göttingen, Germany
(Received 8 July 2005; revised manuscript received 15 December 2005; published 17 March 2006)

The determination of electric field distributions within superconductors is of fundamental importance for both basic research and applications. The analysis of electric fields allows insights into different modes of vortex dynamics in superconductors as well as the determination of local maxima of dissipation which could destabilize superconducting transport. We present an analysis of electric field distributions for thin films in magnetization experiments. We show that electric field distributions can be determined experimentally by time-resolved magneto-optical measurements of flux density distributions via the Faraday law. We give a detailed analysis of the inductive and the potential contributions to the electric fields $\mathbf{E}_i$ and $\mathbf{E}_p$, respectively. Experimental results are demonstrated for a magnetized square-shaped $YBa_2Cu_3O_{6.95}$ thin film.

DOI: 10.1103/PhysRevB.73.094508 PACS number(s): 74.25.Qt, 74.78.Bz

I. INTRODUCTION

The most remarkable phenomenon of superconducting materials is the sharp drop of the resistivity of an electric current to an unmeasureable small value at a critical temperature T_c. This is inevitably related to the screening of electric fields. Since an electric field corresponds to a time change of the phase of an electron wave, the macroscopic phase coherence of the superconducting condensate is incompatible with an electric field. However, it is well known that in type-II superconductors a current-induced motion of the Abrikosov flux lines (vortices) induces electric fields.[1–3] The preservation of true superconducting currents requires pinning of flux lines at materials defects. In high-temperature superconductors (HTS's) the interplay of intrinsic anisotropy and large thermal fluctuations enhances strongly the thermally activated depinning and motion of vortices. Dependent on materials properties and experimental conditions, a variety of different regimes of vortex motion, such as thermally activated flux creep (TAFC),[4] current-induced plastic creep,[5] or flux flow (FF) can be observed. Their relation to different modes of vortex dynamics like collective creep,[6] moving vortex bundles and chains,[7] flux avalanches,[8] self-organized vortex motion,[9] or even the occurrence of instabilities[10] is topic of actual research.

There are excellent theoretical studies of electric field distributions of superconductors in magnetization[11–13] and transport experiments.[14,15] Gurevich and Brandt predict a universal spatial pattern of the electric field in magnetization experiments, which only depends on the sample geometry.[12,13] For transport currents, regions of strongly inhomogeneous electric fields are predicted by Gurevich and Friesen.[15] The theoretical work has in common that it is based on a materials law which is assumed to be valid in the entire superconductor.[16] However, different collective modes of vortex motion (like avalanches, glassy creep, or vortex dynamics at weak links) should be inevitably related to different electric field patterns. Therefore, it is highly desirable to gain experimental insight into the electric field distributions of superconductors[17] which is not based on the application of a materials law. Work that direction on $YBa_2Cu_3O_7$ and $Nd_{1.85}Ce_{0.15}CuO_4$ single crystals has been performed by Giller *et al.*[18] There, a one-dimensional approximation for the calculation of the electric field $\mathbf{E}$ from measured time evolutions of the flux density was used. For the study of the electric field and the vortex dynamics at specific locations, like current domain boundaries, grain boundaries, flux filaments at large defects, or avalanches, where anomalies of the vortex motion are expected, a more general method has to be applied. Our own first approach[17] to generalize electric field imaging to two-dimensional current distributions is based on incorrect approximations. For the integration of the Faraday law, it disregards the contribution of the time evolution of the external stray field of the sample to the inductive electric field which, however, represents the dominant contribution.

In this article, we consider the *true* total electric field of a superconductor. The true electric field is induced by moving vortices or by temporal evolution of the supercurrent density. Theoretical work suggests the existence of an *effective* electric field, where thermodynamic contributions and the Bernoulli potential are considered[19,20]. The contribution of such an effective electric field, if present, is extremely small because it is related to surface inhomogeneities of the superconducting state, such as vortex cores. If such an effective electric field would exist in a superconductor, it would be by orders of magnitude smaller than the true electric field caused by vortex motion. In particular this applies to high-T_c superconductors, which have an extremely small coherence length and the spatial extent of surface inhomogeneities is very small.

The total true electric field $\mathbf{E}$ is comprised of the inductive $\mathbf{E}_i$ and the potential contribution $\mathbf{E}_p$. The determination of $\mathbf{E}_i(\mathbf{r})$ via the induction law requires the measurement of the time evolution of the magnetic flux density vector $\mathbf{B}(\mathbf{r})$ in the entire space inside and outside the sample. Since this is not possible for arbitrary sample geometries, the method for the determination of $\mathbf{E}(\mathbf{r})$ presented in this article is restricted to magnetization experiments of thin-film superconductors with arbitrary shape. For the case of a two-dimensional current distribution $\mathbf{j}(x,y)$, the inversion of the Biot-Savart law allows an unambiguous determination of the current density from the measured normal component of the flux density

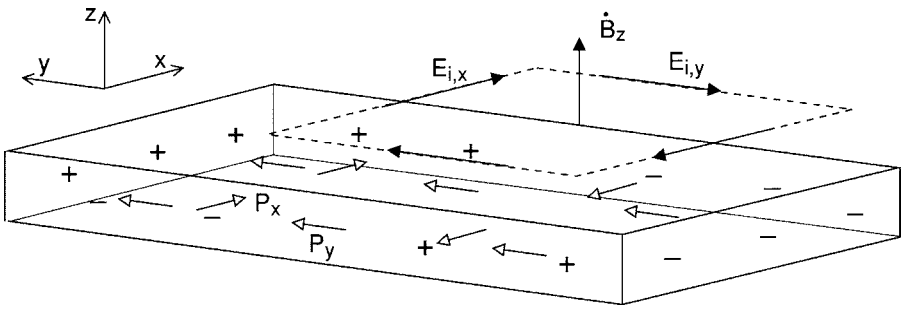

FIG. 1. Sketch of an electrically polarizable sample in an inductive electric field $\mathbf{E}_i$, which is induced by a local temporal evolution of B_z. According to the Faraday law, electric field components $E_{i,x}$ and $E_{i,y}$ are induced along any contour containing $\dot{B}_z \neq 0$ (black arrows). This inductive field $\mathbf{E}_i$ polarizes the medium, and consequently a polarization field $\mathbf{P}$ (white arrows) and a charge density $n^{in}=-\epsilon_0 \nabla \cdot \mathbf{P}$ are induced in the sample (here only depicted at the sample surfaces). The induced charge density is the source of a potential electric field $\mathbf{E}_p=-\mathbf{P}$ in the sample.

$B_z(x,y)$ at the surface of the superconductor.[21] The determination of the time evolution of $\mathbf{j}(x,y,t)$ by experiment is the starting point for the calculation of the time evolution of the flux density components $\mathbf{B}(\mathbf{r},\mathbf{t})=(B_x(\mathbf{r},t),B_y(\mathbf{r},t),B_z(\mathbf{r},t))$ inside and outside the superconducting film and therefore for the calculation of $\mathbf{E}_i(\mathbf{r})$. The potential contribution $\mathbf{E}_p(\mathbf{r})$ can be derived from the obtained $\mathbf{E}_i(\mathbf{r})$ and $\mathbf{j}(x,y)$ distributions.

The article is organized as follows: In Sec. II we present the general electrodynamics of superconductors for the determination of inductive and potential contributions to $\mathbf{E}(\mathbf{r})$. Solutions of the equations are derived for a relaxing two-dimensional (2D) current distribution in thin films in Sec. III. Section IV presents the special case of a relaxing one-dimensional current distribution and calculates the electric field distribution in the cross section of a thin stripe. Section V presents an exemplary experimental study of the time decay of the flux density gradients of a magnetized square-shaped YBaCuO thin film. The two-dimensional inductive electric field distribution in the film plane is calculated via two-dimensional Fourier transformations. In Sec. VI, it is shown that the dielectric polarization field $\mathbf{P}(\mathbf{r})$, the potential electric field $\mathbf{E}_p(\mathbf{r})$, and the induced charge density distribution $n^{in}(\mathbf{r})$ can be determined.

II. THEORY

In superconductors, an electric field distribution is induced by moving vortices[1] or (e.g., in the vortex free Meissner phase) by a temporal evolution of supercurrents.[21] As pointed out in the former section, a possibly existing thermodynamic electric field is disregarded in this article. According to the Faraday law, the time derivative of the microscopic flux density distribution of a moving vortex, $-\dot{\mathbf{b}}(\mathbf{r})=\nabla \times \mathbf{e}_i(\mathbf{r})$, induces a microscopic electric field distribution $\mathbf{e}_i(\mathbf{r})$ with pure inductive origin[1] (the dot indicates the time derivative). In addition to this inductive electric field, a complex dielectric polarization pattern $\mathbf{p}(\mathbf{r})$ and thus a potential electric field are $\mathbf{e}_p(\mathbf{r})$ induced due to the redistribution of the electric charge density in the area of the vortex core. As already pointed out by Bardeen and Stephen,[1] $\mathbf{e}(\mathbf{r})$ gives rise to an acceleration of quasiparticles in the vortex core and, consequently, an electric displacement charge density $n^{in}(\mathbf{r})$ is induced in a region of the size of the vortex core, with $\epsilon_0 \nabla \cdot \mathbf{p}(\mathbf{r})=-n^{in}(\mathbf{r})$. Therefore, a moving vortex represents an electric dipole.[22] Recent work[23] gives some evidence that even a vortex at rest may accumulate some charge (of the order of 0.01 electron charges in $YBa_2Cu_3O_7$) possibly due to the mentioned thermodynamic potential—i.e., the difference of the chemical potential inside and outside the vortex core. Both kinds of charges at the vortex core are screened on the length scale of several coherence lengths, and the entire vortex represents an electrically neutral object.

The aim of this article is the determination of mesoscopic electric field distributions related to the collective motion of a large number of vortices. Although the details of the microscopic $\mathbf{p}(\mathbf{r})$ pattern near the vortex core are not important for the mesoscopic electric field distributions, it is necessary to notice that a superconductor in the vortex state represent an electrically polarizable medium. The electromagnetic quantities of superconductors on a mesoscopic length scale are defined as a local spatial average over the microscopic properties of ensembles of individual vortices. The flux density $\mathbf{B}(\mathbf{r})=\langle \mathbf{b}(\mathbf{r}) \rangle_a$ then represents a spatial average over an area a^2 which is determined by the spatial resolution a of an experimental setup and may contain some vortices up to hundreds of vortices, depending on a and the vortex density. This mesoscopic length scale has an important physical significance, since real transport supercurrents in the vortex state develop as a superposition of inhomogeneously distributed microscopic eddy currents of vortices.[24] The time evolution of the mesoscopic flux density $\mathbf{B}(r)$ then gives insights into the spatial structure of the electric field $\mathbf{E}(\mathbf{r})=\langle \mathbf{e}(\mathbf{r}) \rangle_a$ on the same length scale. Furthermore, we introduce a mesoscopic average of the dielectric polarization vector $\mathbf{P}(\mathbf{r})=\langle \mathbf{p}(\mathbf{r}) \rangle_a$. $\mathbf{P}(\mathbf{r})$ may be important at areas of strongly nonuniform motion of vortex ensembles (such as sample edges or current domain boundaries). In contrast, for a uniformly moving vortex lattice all microscopic dipoles cancel—i.e., $\mathbf{P}(\mathbf{r})=0$.

All microscopic effects of the generation of the true electric field in superconductors are fully contained in the Maxwell theory for the mesoscopic quantities. The electric induction field $\mathbf{E}_i(\mathbf{r})$ is derived from the time derivative of the magnetic induction $\dot{\mathbf{B}}(\mathbf{r})$ via the Faraday law

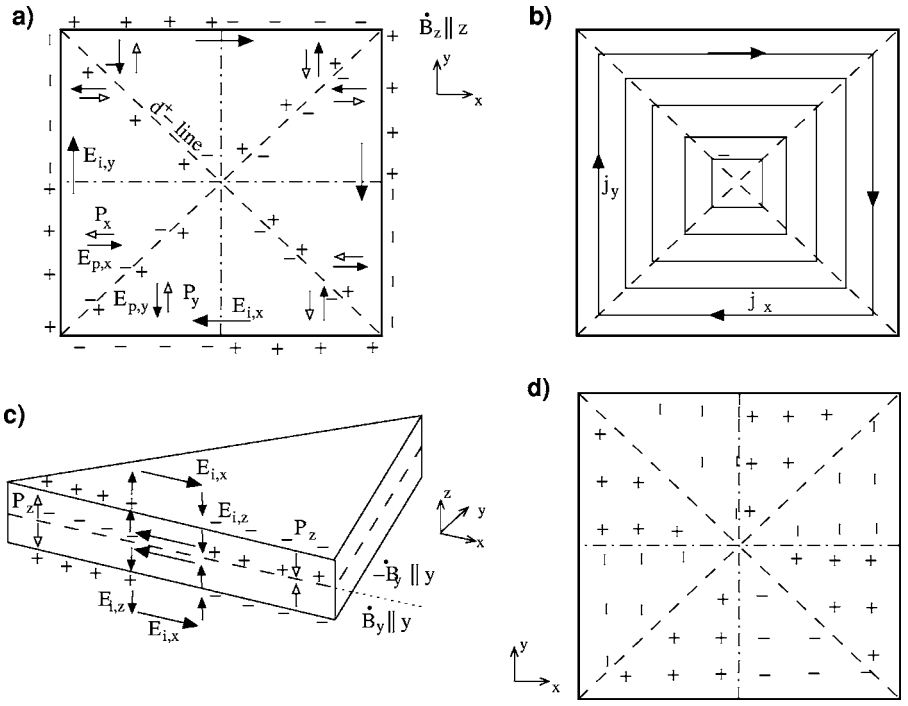

FIG. 2. Sketch of the induced surface charge densities n_s^{in} due to electric field components perpendicular to a relaxing current density. (a) Contribution of the relaxation of the normal flux density component $\dot{B}_z$ to the electric field in the (x,y) plane of a square-shaped film with a relaxing Bean-like current density (b) (bold lines represent current flow lines). According to the Faraday law, in each current domain, there are inductive electric field components parallel and perpendicular to the current density. Whereas the $\mathbf{E}_i$ component $\|\mathbf{j}$ reflects the occurrence of a finite resistivity, the $\mathbf{E}_i$ component perpendicular to $\mathbf{j}$ induces a charge density and a polarization $\mathbf{P}$ which is related to inhomogeneous vortex motion. Note that the total electric field $\mathbf{E}_i+\mathbf{E}_p$ (with $\mathbf{E}_p=-\mathbf{P}$) is parallel to the current density. (c) Possible occurrence of an E_z component of the inductive electric field due to the relaxation of in-plane flux densities. Shown is a j_x domain of a square-shaped film with a $\partial_t B_y$. Since the total electric field must be parallel to $\mathbf{j}$, E_z is totally canceled by $E_{p,z}$ due to surface charge densities at the $z=\pm d/2$ [see (d)] and the $z=0$ planes.

$$\frac{\partial \mathbf{B}}{\partial t} = -\nabla \times \mathbf{E}_i. \tag{1}$$

The inductice electric field $\mathbf{E}_i$ has pure rotational character and consequently $\nabla \cdot \mathbf{E}_i(\mathbf{r})=0$. In electrically polarizable media or media with mobile charges, the inductive electric field $\mathbf{E}_i(\mathbf{r})$ gives rise to a dielectric polarization field $\mathbf{P}(\mathbf{r})$ (see Fig. 1 for the general case of a polarizable medium in a time-dependent field and Fig. 2 for the case of flux creep in a square-shaped superconductor in a fully penetrated state). $\mathbf{P}(\mathbf{r})$ is related to induced volume and surface charge densities $n^{in}(\mathbf{r})$ via $\epsilon_0 \nabla \cdot \mathbf{P} = -n^{in}$. Due to the presence of $n^{in}(\mathbf{r})$, a potential electric field $\mathbf{E}_p(\mathbf{r})$ is generated with $\epsilon_0 \nabla \cdot \mathbf{E}_p = n^{tot} = n^{ex} + n^{in}$, where n^{ex} represents any excess or external charge density. If $n^{ex}=0$, $\mathbf{E}_p(\mathbf{r})=-\mathbf{P}(\mathbf{r})$ inside the sample. Note, that the spatial average of the induced charge density in the entire sample $\langle n^{in}(\mathbf{r})\rangle = 0$.[11] The total electric field is then (according to the Helmholtz decomposition) comprised of two contributions $\mathbf{E}=\mathbf{E}_i+\mathbf{E}_p$, where $\mathbf{E}_i$ has inductive and $\mathbf{E}_p=-\nabla\phi$ has potential character—i.e., $\nabla \times \mathbf{E}_p = \nabla \times \nabla \phi = 0$ with $\Delta\phi = -n^{in}/\epsilon_0$ and $\nabla \cdot \mathbf{E}_i = 0$.

The dielectric displacement $\mathbf{D}=\epsilon_0 \epsilon \mathbf{E}_{tot}$ is given by

$$\mathbf{D} = \epsilon_0 \mathbf{E}_i + \epsilon_0 \mathbf{E}_p + \epsilon_0 \mathbf{P}, \tag{2}$$

with

$$\nabla \cdot \mathbf{D} = n^{ex}. \tag{3}$$

Consequently, $\mathbf{D}$ is independent of the considered material and just depends on the electric induction field $\mathbf{E}_i$ and the excess charge density n^{ex}—e.g., due to external charges.

The boundary conditions according to the Maxwell theory require the continuity of the tangential components of $\mathbf{E}$ at all surfaces. In contrast, the normal components of $\mathbf{E}$ exhibit discontinuities due to the presence of surface charge densities. In the following, we restrict our analysis to magnetization experiments of electrically isolated samples, where external charges or potentials are absent—i.e., $\nabla \cdot \mathbf{D}=0$ and $\phi=0$ at the surface of the sample. The time evolution of the magnetic flux density is then comprised of $\mathbf{B}(\mathbf{r},t) = \mu_0 \mathbf{H}_{ex}(t) + \mu_0 \mathbf{H}(\mathbf{r},t)$, where $\mu_0 \mathbf{H}_{ex}$ represents the contribution of the external field and the magnetic field $\mathbf{H}(\mathbf{r})$ is generated by the flowing supercurrents:

$$\nabla \times \mathbf{H} = \frac{\partial \mathbf{D}}{\partial t} + \mathbf{j}. \tag{4}$$

Usually, electric fields in superconductors are extremely small and thus the contribution of the time derivative of the electric displacement $\partial \mathbf{D}/\partial t$ to the magnetic field in Eq. (4) can be completely disregarded. For the magnetic induction one has

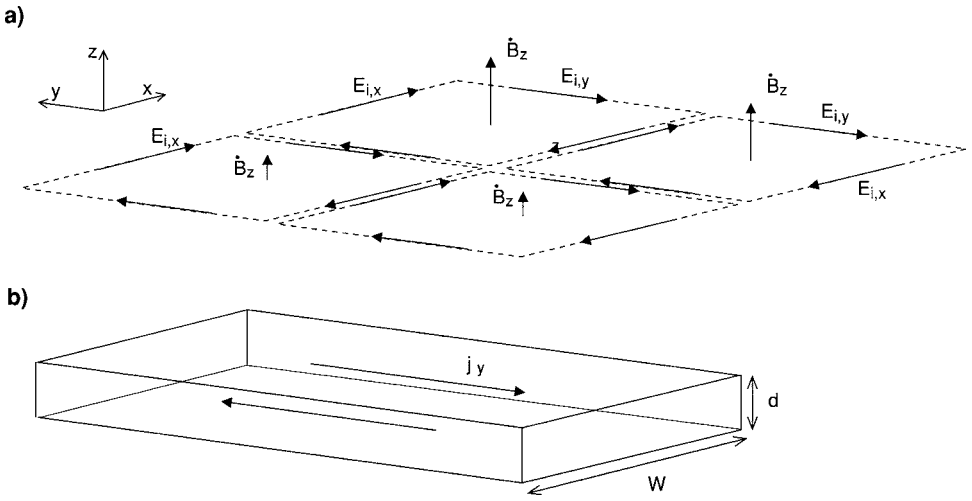

FIG. 3. (a) Scheme for the integration of the Faraday law according to the Stokes theorem. If the integration area is divided into cells, each containing a time change of the flux density component B_z, the electric field components can be calculated along the contours of each cell. However, the neighboring cells have to be taken into account. (b) Strip geometry for the one-dimensional current distribution.

$$\nabla \cdot \mathbf{B} = 0. \tag{5}$$

In magnetization experiments, the time evolution of the flux density $\mathbf{B}(\mathbf{r},t)$ according to Eqs. (4) and (5) is directly related to the time evolution of the current density $\mathbf{j}(\mathbf{r},t)$ and the time evolution $\mu_0 \mathbf{H}_{ex}(t)$. After ramping of H_{ex} is stopped, the time evolution of $\mathbf{j}(\mathbf{r},t)$ determines the time evolution of $\mathbf{B}(\mathbf{r},t)$, only.

The key step for the determination of the total electric field distribution $\mathbf{E}$ in superconductors during magnetization experiments is the integration of the Faraday law [Eq. (1)] in order to obtain the inductive electric field $\mathbf{E}_i(\mathbf{r})$. There are two alternative approaches to calculate the $\mathbf{E}_i(\mathbf{r})$ which exactly give the same results. One approach is the introduction of a vector potential $\mathbf{X}(\mathbf{r})$ with

$$\mathbf{E}_i = \nabla \times \mathbf{X}. \tag{6}$$

This ansatz automatically fulfills $\nabla \cdot \mathbf{E}_i(\mathbf{r}) = 0$ and yields (see Appendix A)

$$\mathbf{E}_i = \frac{1}{4\pi} \int \frac{\dot{\mathbf{B}} \times (\mathbf{r} - \mathbf{r}')}{|\mathbf{r} - \mathbf{r}'|^3} d^3 r'. \tag{7}$$

A second approach (for $\partial_t H_{ex} = 0$) is obtained by applying $\nabla \times$ to Eq. (1) and using Ampères law [Eq. (4)]:

$$\mu_0 \partial_t \mathbf{j} = -\nabla \times \nabla \times \mathbf{E}, \tag{8}$$

where ∂_t stands for $\partial / \partial t$. A similar equation is discussed in the article of Gurevich and Friesen[15] (see also Ref. 11), where, however, $\partial_t \mathbf{j}$ is replaced by $\sigma \partial_t \mathbf{E}$ and thus the nonlinear differential conductivity $\sigma(E) = \partial j / \partial E$ appears as a material law. In our equation (8), no material law is entering.

III. $\mathbf{E}_i$ FOR 2D CURRENT DISTRIBUTIONS

In this section, the reconstruction of the inductive electric field in superconductors with a relaxing two-dimensional current distribution $\mathbf{j}(x,y,t) = j_x(x,y,t)\mathbf{e_x} + j_y(x,y,t)\mathbf{e_y}$ is considered. This is the case in thin-film samples in a perpendicular external magnetic field. The z dependence of the current density $\mathbf{j}(x,y)$ can be disregarded for film thickness $d \leqslant \lambda$, where λ represents the London penetration depth—i.e., the length scale of the spatial variation of the superconducting current density. This represents a completely two-dimensional problem for the current density. However, with respect to the magnetic flux density and the electric field distribution, the problem remains three dimensional.

A. In-plane components of $\mathbf{E}_i$

After two-dimensional Fourier transformation of Eq. (7) (see Appendix B), the Fourier coefficients of the $E_{i,x}(\mathbf{r})$ component of the electric field are given by

$$\tilde{E}_{i,x}(k_x,k_y,z) = \tilde{E}^{(1)}_{i,x} + \tilde{E}^{(2)}_{i,x}, \tag{9}$$

with

$$\tilde{E}^{(1)}_{i,x} = \int_{-\infty}^{\infty} dz' g(k_x,k_y,z,z') \tilde{\dot{B}}_y(k_x,k_y,z') \tag{10}$$

and

$$\tilde{E}^{(2)}_{i,x} = -\int_{-\infty}^{\infty} dz' l(k_x,k_y,z,z') \tilde{\dot{B}}_z(k_x,k_y,z'). \tag{11}$$

Similarly, the Fourier coefficients of $E_{i,y}(\mathbf{r})$ are given by

$$\tilde{E}_{i,y}(k_x,k_y,z) = \tilde{E}^{(1)}_{i,y} + \tilde{E}^{(2)}_{i,y}, \tag{12}$$

with

$$\tilde{E}^{(1)}_{i,y} = \int_{-\infty}^{\infty} dz' h(k_x,k_y,z,z') \tilde{\dot{B}}_z(k_x,k_y,z') \tag{13}$$

and

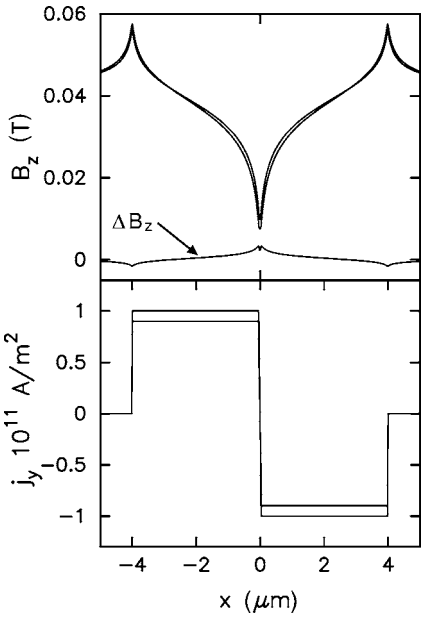

FIG. 4. Calculated temporal change of the normal magnetic flux component $B_z(x)$ of a thin strip of thickness $d=200$ nm, width $W=8$ μm in an external magnetic field of $\mu_0 H=42$ mT. The strip is in a nearly fully penetrated state and carries a constant magnetization current density with a value of $j_c(t_1)=\pm 10^{11}$ A/m^2 which relaxes to $j_c(t_2)=\pm 0.9\times 10^{11}$ A/m^2. $\Delta B_z=B_z(t_2)-B_z(t_1)$ denotes the corresponding change of the flux density.

$$\tilde{E}^{(2)}_{i,y}=-\int_{-\infty}^{\infty} dz'\, g(k_x,k_y,z,z')\dot{\tilde{B}}_x(k_x,k_y,z'). \tag{14}$$

For the Fourier-transformed integral kernels see Appendix B.

The key step for our thin-film method is to express the Fourier coefficients $\dot{\tilde{B}}(k_x,k_y,z)$ of the time derivate of the flux density via the Fourier coefficients of the time derivative of the two-dimensional current density $\partial_t\tilde{j}_x(k_x,k_y)$ and $\partial_t\tilde{j}_y(k_x,k_y)$. This is possible by using a two-dimensional Fourier-transformed version of the Biot-Savart law (see Appendix C).

For the determination of the Fourier coefficients of the $E_{i,x}$ component of the electric field, we then calculate the two contributions in Eq. (9) separately and obtain nonanalytical expressions (see Appendix D). However, for the $z=0$ plane, where the in-plane electric field has a global maximum, the following analytical expressions are found:

$$\tilde{E}^{(1)}_{i,x}(k_x,k_y,z)=\frac{\mu_0}{4k^2}\partial_t\tilde{j}_x(k_x,k_y)\{e^{-kd/2}(dk+1)-e^{kd/2}\} \tag{15}$$

and

$$\tilde{E}^{(2)}_{i,x}(k_x,k_y,z)=-\frac{\mu_0}{4}\frac{k_y}{k^2}\dot{\alpha}\left\{\frac{2}{k}\sinh\left(\frac{kd}{2}\right)e^{-kd}-\frac{1}{k}\{5e^{kd}+dke^{kd}-1-4e^{3/2kd}\}e^{-3/2kd}\right\}, \tag{16}$$

with

$$\dot{\alpha}=\frac{k_y}{k}\partial_t\tilde{j}_x(k_x,k_y,z')-\frac{k_x}{k}\partial_t\tilde{j}_y(k_x,k_y,z') \tag{17}$$

and wave number $k=\sqrt{k_x^2+k_y^2}$.

We now apply the thin-film approximation $kd\leqslant 1$, where the lateral measurement resolution k_{max}^{-1} is comparable or worse than the film thickness d. Typically, $d\leqslant 300$ nm and $k_{max}^{-1}\approx 1-3$ μm in our experiments. Using the first-order approximation $e^x\approx 1+x$ we obtain

$$\tilde{E}_{i,x}(k_x,k_y,z=0)=-\frac{\mu_0 d^2}{8}\partial_t\tilde{j}_x(k_x,k_y)+\frac{\mu_0}{2k}\frac{k_y}{k^2}\sinh\left(\frac{kd}{2}\right)\dot{\alpha}. \tag{18}$$

Similarly the total inductive E_y can be calculated, giving

$$\tilde{E}_{i,y}(k_x,k_y,z=0)=-\frac{\mu_0 d^2}{8}\partial_t\tilde{j}_y(k_x,k_y)-\frac{\mu_0}{2k}\frac{k_x}{k^2}\sinh\left(\frac{kd}{2}\right)\dot{\alpha}. \tag{19}$$

B. Normal component of $\mathbf{E}_i$

The Fourier coefficients of the perpendicular inductive component of the electric field $E_{i,z}$ are given by (see AppendixB)

$$\tilde{E}_{i,z}(k_x,k_y,z)=\frac{\mu_0}{4k^2}\{ik_x\partial_t\tilde{j}_x+ik_y\partial_t\tilde{j}_y\}\zeta(z,k,d), \tag{20}$$

with

$$\zeta(z,k,d)=\int_{-\infty}^{\infty} dz'\, e^{-k|z-z'|}\{e^{-k|z'-d/2|}-e^{-k|z'+d/2|}\}. \tag{21}$$

Since $ik_x\partial_t\tilde{j}_x+ik_y\partial_t\tilde{j}_y$ is the Fourier-space equivalent for $\nabla\cdot\partial_t\mathbf{j}=-\ddot{n}^{in}$, Eq. (20) shows that an $E_{i,z}$ component is present only if $\ddot{n}^{in}\neq 0$—i.e., if the change of the rate of flux creep in time is large enough. In this article, where our method is applied to slowly relaxing magnetized films, $\ddot{n}^{in}$ can be completely disregarded. Furthermore, the ζ function displays a sign reversal at the $z=0$ plane and one has $E_{i,z}(z=0,k,d)=0$ for arbitrary $\ddot{n}^{in}$ values.

C. Alternative approach for the in-plane components of $\mathbf{E}_i$

In this section, we show that the in-plane components of the inductive electric field can also be easily obtained if we start from Eq. (8) and apply a thin-film approximation, where the z dependence of the two-dimensional current density $\mathbf{j}(x,y)$ is disregarded. Writing down Eq. (8) in components, using $\dot{B}_z=-\partial_x E_{i,y}+\partial_y E_{i,x}$, and summarizing some terms yields

$$\begin{aligned}\partial_z^2 E_{i,x}&=-\partial_y\dot{B}_z+\mu_0\partial_t j_x+\partial_x\partial_z E_{i,z},\\ \partial_z^2 E_{i,y}&=\partial_x\dot{B}_z+\mu_0\partial_t j_y+\partial_y\partial_z E_{i,z},\\ (\partial_x^2+\partial_y^2)E_{i,z}&=\partial_z\partial_x E_{i,x}+\partial_z\partial_y E_{i,y}=0.\end{aligned} \tag{22}$$

According to the result in the former section that the E_z component is small for slow changes in the relaxation rate, in

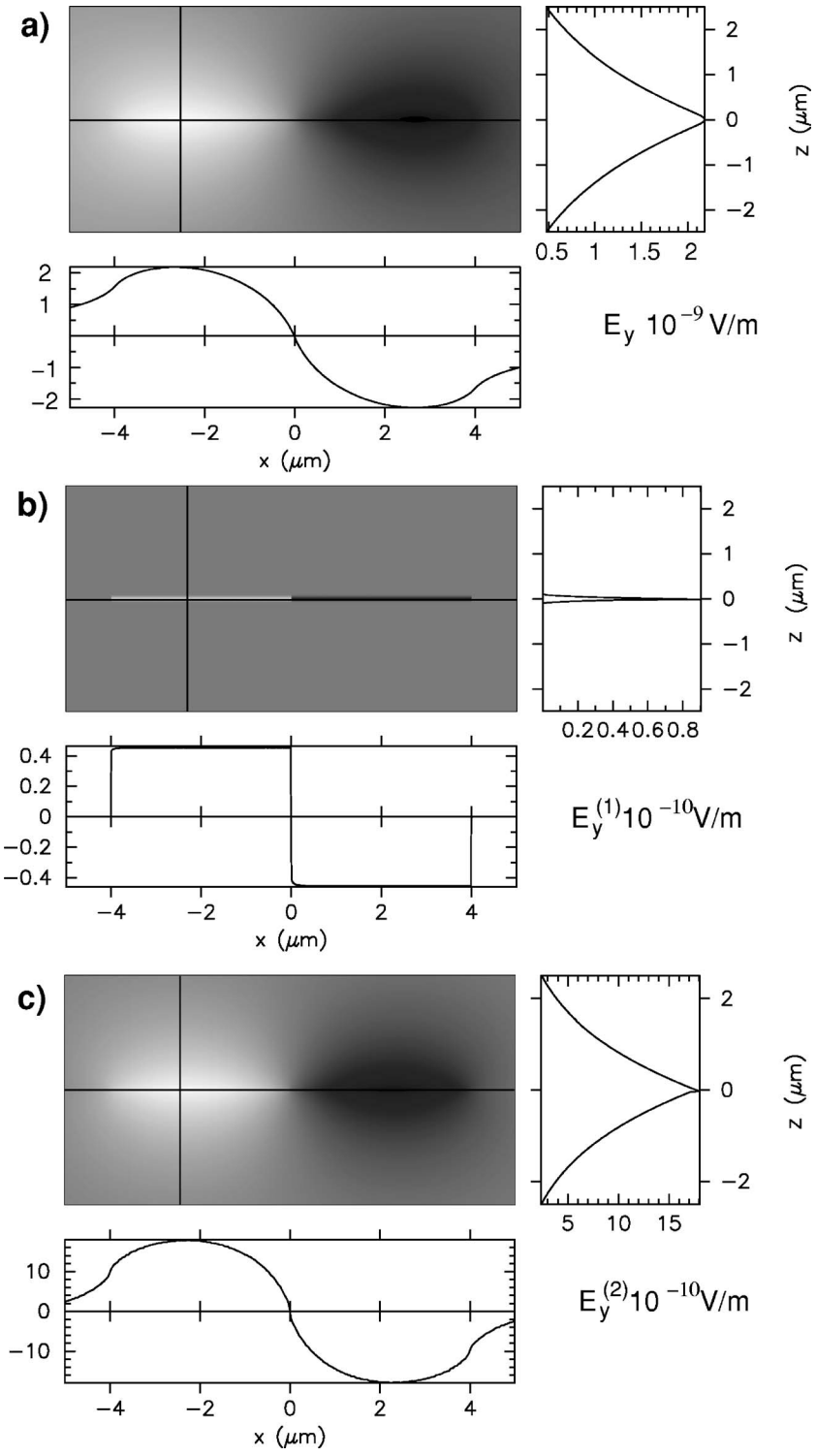

FIG. 5. Different contributions to the total inductive electric field in the (x,z) plane of a thin-film strip being extended infinitely in the y direction. The strip is in a fully penetrated state and the time evolution of the flux and current distribution are shown in Fig. 4. (a) Total inductive electric field $E_{i,y}$ according to Eq. (28) for $|\partial_t j_y| = 10^{10}$ A/(m^2 sec). In (b) and (c) the two contributions to the inductive electric field distribution according to Eqs. (31) and (32) are depicted. Note that the size of the cross section of the strip ($W/d=40$) can be seen in the grey-scale pattern of (b).

the following, the $E_{i,z}$ component in Eq. (22) will be disregarded. This allows a decoupling of the solution of Eq. (22) for the E_x and E_y components, respectively, and thus

$$\partial_z^2 E_{i,x} = -\partial_y \dot{B}_z + \mu_0 \partial_t j_x,$$

$$\partial_z^2 E_{i,y} = \partial_x \dot{B}_z + \mu_0 \partial_t j_y. \tag{23}$$

In the thin-film limit, the integration of Eq. (23) yields

$$E_{i,x}(x,y,z) = \mu_0 \partial_t j_x(x,y)\left(\frac{z^2}{2} - \frac{d^2}{8}\right) - \int_{-\infty}^{z} d^2 z' \partial_y \dot{B}_z,$$

$$E_{i,y}(x,y,z) = \mu_0 \partial_t j_y(x,y)\left(\frac{z^2}{2} - \frac{d^2}{8}\right) + \int_{-\infty}^{z} d^2 z' \partial_x \dot{B}_z. \tag{24}$$

For a discussion of the integration method see the next section. After two-dimensional Fourier transformation in the

(x,y) plane and expressing the Fourier components of B_z via the Fourier components of the current density (see Appendix C) the Fourier components of the electric field are written

$$\tilde{E}_{i,x}(k_x,k_y,z) = \mu_0 \partial_t \tilde{j}_x(k_x,k_y,t)\left[\frac{z^2}{2} - \frac{d^2}{8}\right] + \frac{\mu_0}{2k}\frac{k_y}{k^2}\sinh\left(\frac{kd}{2}\right)\dot{\alpha}e^{-k|z|},$$

$$\tilde{E}_{i,y}(k_x,k_y,z) = \mu_0 \partial_t \tilde{j}_y(k_x,k_y,t)\left[\frac{z^2}{2} - \frac{d^2}{8}\right] - \frac{\mu_0}{2k}\frac{k_x}{k^2}\sinh\left(\frac{kd}{2}\right)\dot{\alpha}e^{-k|z|}, \quad (25)$$

where $\dot{\alpha}$ is defined in Eq. (17). Note that $\mathbf{j}=0$ for $|z|>d/2$. For the electric field distribution in the central plane $z=0$ of the superconductor we recover then Eqs. (18) and (19).

IV. SOLUTIONS AND TESTS FOR 1D CURRENT DISTRIBUTIONS

In order to improve our understanding of the electric field distributions, in this section, Eq. (24) is compared to a direct integration of Eq. (1) for superconducting samples with one-dimensional current distribution $j_y(x)$—i.e., a thin strip which is extended infinitely in the y direction. The strip has a width W (parallel to the x direction) and a thickness d [see Fig. 3(b)]. As before, we consider only magnetization experiments. The current loop is closing at infinity and no external potentials or charges are present. The only electric field component in this case is the $E_{i,y}$ component; $E_{i,x}$ and $E_{i,z}$ in this artificial geometry are zero everywhere. Since $\mathrm{div}\,\mathbf{E}=\partial_y E_y = 0$, no charge density is induced in the sample and therefore $\mathbf{P}$ and $\mathbf{E}_p$ are zero.

Generally, the Faraday law, Eq. (1), is integrated by means of the Stokes theorem. This is related to the integral representation of the Faraday law

$$\int_A d^2r' \dot{\mathbf{B}}(\mathbf{r}') = -\oint_C \mathbf{ds}\cdot\mathbf{E}_i. \quad (26)$$

As an example, we consider now the case that only a time derivative of B_z is present [see Fig. 3(a)]. We divide our integration area in small cells with area a^2 and contour C with length $4a$, each cell exhibiting a locally piecewice constant $\dot{B}_z$. The electric field components $E_{i,x}$ and $E_{i,y}$ due to the local flux change $\dot{B}_z$ in an isolated cell are then approximately given by $E_{i,x}=E_{i,y}\approx \dot{B}_z a/4$. However, also the flux changes in each neighbor cell have to be taken into account. If we now consider the one-dimensional case with $E_{i,x}=0$ and reduce the cell size to the limit of continuous $\dot{B}_z(x)$ distributions, the calculation of the $E_{i,y}$ component of the electric field can be performed by a single integration of $\dot{B}_z(x)$ along the x direction.

This can be also derived directly from Eq. (1). The differential form of the Faraday law, Eq. (1), for the one-dimensional case is written

$$\dot{B}_x(x,z) = \partial_z E_{i,y}(x,z),$$

$$\dot{B}_z(x,z) = -\partial_x E_{i,y}(x,z). \quad (27)$$

Due to $\mathrm{div}\,\mathbf{B}=0$, $E_{i,y}$ along a given contour C is independent of the choice of the integration area A (as long as $\partial A = C$) and consequently the two lines of Eqs. (27) are equivalent. The solution of Eqs. (27) is, e.g., given by

$$E_{i,y}(x,z) = -\int_{-\infty}^{x} dx' \dot{B}_z(x',z), \quad (28)$$

where the lower integration bound has to be chosen in an area without flux changes. This result immediately shows that the electric field in the strip is induced by all flux changes inside and outside the sample. Consequently, the integral in Eq. (28) should be taken over the full spatial extent of the self-field of the sample. Therefore, the electric field $\mathbf{E}_i(x,y)$ at a specific location in the samples depends nonlocally on the flux changes inside and outside the superconductor strip.

In order to shed light on our solution of the two-dimensional problem [Eqs. (24)], it is shown in the following how the second line of Eqs. (24) can be also obtained from Eq. (27) in the 1D geometry. Applying ∂_z to the first line of Eqs. (27) and using Eq. (4), $\mu_0 \partial_t j_y = \partial_z \dot{B}_x - \partial_x \dot{B}_z$, we recover the second line of Eqs. (23)

$$\partial_z^2 E_{i,y} = \partial_x \partial_t B_z + \mu_0 \partial_t j_y. \quad (29)$$

The integration of this equation, assuming a z-independent current density in the film, yields

$$E_{i,y}(x,z) = E_{i,y}^{(1)}(x,z) + E_{i,y}^{(2)}(x,z), \quad (30)$$

with a contribution being directly related to the current relaxation

$$E_{i,y}^{(1)}(x,z) = \mu_0 \partial_t j_y(x)\left(\frac{z^2}{2} - \frac{d^2}{8}\right). \quad (31)$$

Note that $j_y=0$ for $|z|>d/2$ and therefore $E_{i,y}^{(1)}=0$ outside the sample. The second contribution is nonlocal and is related to an integral of the gradient of $\partial_t B_z$,

$$E_{i,y}^{(2)}(x,z) = \int_{-\infty}^{z} d^2z' \partial_x \partial_t B_z. \quad (32)$$

Note that the sum of Eqs. (31) and (32) exactly corresponds to Eq. (28). This will be visualized in the following for simple relaxing model current distributions.

A. Numerical results for model current distributions

In this section, numerical results of Eqs. (28) and (30), respectively, are calculated by using theoretical Bean-model-like current distributions for the infinitely extended thin strip. We want to shed light on the relative strength of different contributions to the total electric field in Eq. (30). Results for a partly penetrated state are presented, where the shrinking of the Meissner area during magnetic relaxation and the contri-

bution of the time evolution of the Meissner currents have to be taken into account.

In the thin-film Bean model for the strip of thickness d and width W, being extended infinitely in the y direction [see Fig. 3(b)], the current distribution is given by simple analytical expressions.[25] If $H_{ex}\|z$ is increased from the ZFC state, one obtains, for the current density,[26]

$$j_y(x) = \begin{cases} j_c \dfrac{x}{|x|}, & Q \leqslant |x| \leqslant W/2, \\ \dfrac{2j_c}{\pi} \arctan\left[\dfrac{xc}{(Q^2 - x^2)^{1/2}} \right], & |x| < Q, \end{cases} \tag{33}$$

with $c = 2[(W/2)^2 - Q^2]^{1/2}/W$ and Q indicating the penetration depth of the flux front measured from the strip center. The penetration depth of the magnetic flux measured from the strip edge is $P = W/2 - Q$ with

$$Q = \frac{W}{2} \frac{1}{\cosh\left[\dfrac{\pi H_{ex}}{j_c d} \right]}. \tag{34}$$

This one-dimensional current distribution generates a magnetic stray field in and outside the sample, which can be calculated by the Biot-Savart's law:

$$B_x(x,z) = \frac{\mu_0}{2\pi} \int_{-W/2}^{W/2} dx' j_y(x')$$

$$\times F(x,x',z,z = d/2) - F(x,x',z,z = -d/2),$$

with

$$F(x,x',z,z') = \frac{1}{2} \ln[(x - x')^2 + (z - z')^2],$$

$$B_z(x,z) = -\frac{\mu_0}{2\pi} \int_{-W/2}^{W/2} dx' j_y(x')$$

$$\times G(x,x',z,z' = d/2) - G(x,x',z,z' = -d/2),$$

with

$$G(x,x',z,z') = \arctan\left[\frac{z - z'}{x - x'} \right]. \tag{35}$$

Note that in contrast to the analytical solution in Ref. 26 for $d \to 0$, the calculation of **B** in Eq. (35) is performed for strips of finite thickness d, where no analytical solution is known. This is necessary for calculating electric fields inside the strip volume.

Examples of the flux and current distributions are depicted in Figs. 4 and 7 for a fully penetrated and a partly penetrated state. For the calculation of the electric field, it is assumed that the time derivative of the relaxing current density $\partial_t j_y(x) \approx [j_y(x,t_2) - j_y(x,t_1)]/\Delta t \propto j_y(x,t_1)$, where $j_y(x)$ is given by Eq. (33). The corresponding time derivatives of the magnetic flux density components are then calculated by Eq. (35). Finally, the total electric field is calculated by Eq. (28) and is compared with the two different contributions to Eq. (30)—i.e., Eqs. (31) and (32), respectively.

B. Fully penetrated state

The electric field distribution during relaxation of the fully penetrated state in Fig. 4 is depicted in Fig. 5(a). It shows a spatial pattern which is characterized by the following properties: (i) The electric field is maximal in the cross section of the superconducting strip: however, its spatial extend in the z direction is much larger than the thickness of the sample and is of the order of W. (ii) The electric field is parallel to the current density. Consequently, due to the sign change of the current density, $E_{i,y}(x)$ displays a sign reversal at $x = 0$, too, and has an antisymmetric structure with respect to $x = 0$. (iii) Within one current domain, $|E_{i,y}(x)|$ has a maximum value at a distance of $x \approx \frac{2}{3} W/2$ from the sample center. This is approximately the position of the so-called neutral line[28]—i.e., the location where $\dot{B}_z \approx 0$ and $B_z = \mu_0 H_{ex}$.

Very similar results have been obtained before by Gurevich and Brandt[12] and Brandt[13] by a nonlocal diffusion equation for the electric field with a nonlinear current-electric-field material law $E(j) \propto j^m$. They showed that a universal shape of $E_{i,y}(x)$ occurs for strongly nonlinear $E(j)$ $(m \gg 1)$ which only depends on the geometry of the sample. In both references, also analytical results for the x dependence of the electric field are given in the limit $m \gg 1$ in the creep regime. The main new step of this work is that no materials law is applied for the determination of electric field patterns.

The different contributions $E_{i,y}^{(1)}$ and $E_{i,y}^{(2)}$ to the total inductive electric field according to Eqs. (31) and (32) are depicted in Figs. 5(b) and 5(c). As can be nicely seen from a comparison of Fig. 5(a) with Fig. 5(c), the shape of $E_{i,y}^{(2)}$ is similar to the spatial pattern of the total $E_{i,y}$. For the fully penetrated state, $E_{i,y}^{(1)}$ represents only a minor contribution to the inductive electric field.

Since the spatial extend of the magnetic self-field of the strip increases with the sample width W in both the x and z directions, a strong dependence of the total electric field on W is expected.[12] The increase of $E_{i,y}$ with increasing sample width W is shown in Fig. 6, where the electric field distribution in the cross section of three strips with different W is depicted. Note that the thickness is constant ($d = 200$ nm) and all other parameters are unchanged compared to Fig. 4. Independently of W, $E_{i,y}(x,z)$ displays a universal pattern as predicted in Refs. 12 and 13. Whereas d remains constant in Fig. 6, the extent of the $E_{i,y}$ pattern in the z direction increases $\propto W$.

Partly penetrated state

The time evolution of the flux and current density and the corresponding electric field distribution due to current relaxation in a partly penetrated state of a strip strongly differs from that one of a fully penetrated state. Figure 7 shows the change of the flux and current density according to Eqs. (33) and (35). After relaxation of the j_c value by 10%, the penetration depth P of the flux front is increased. Consequently, the Meissner screening current density in the flux-free region

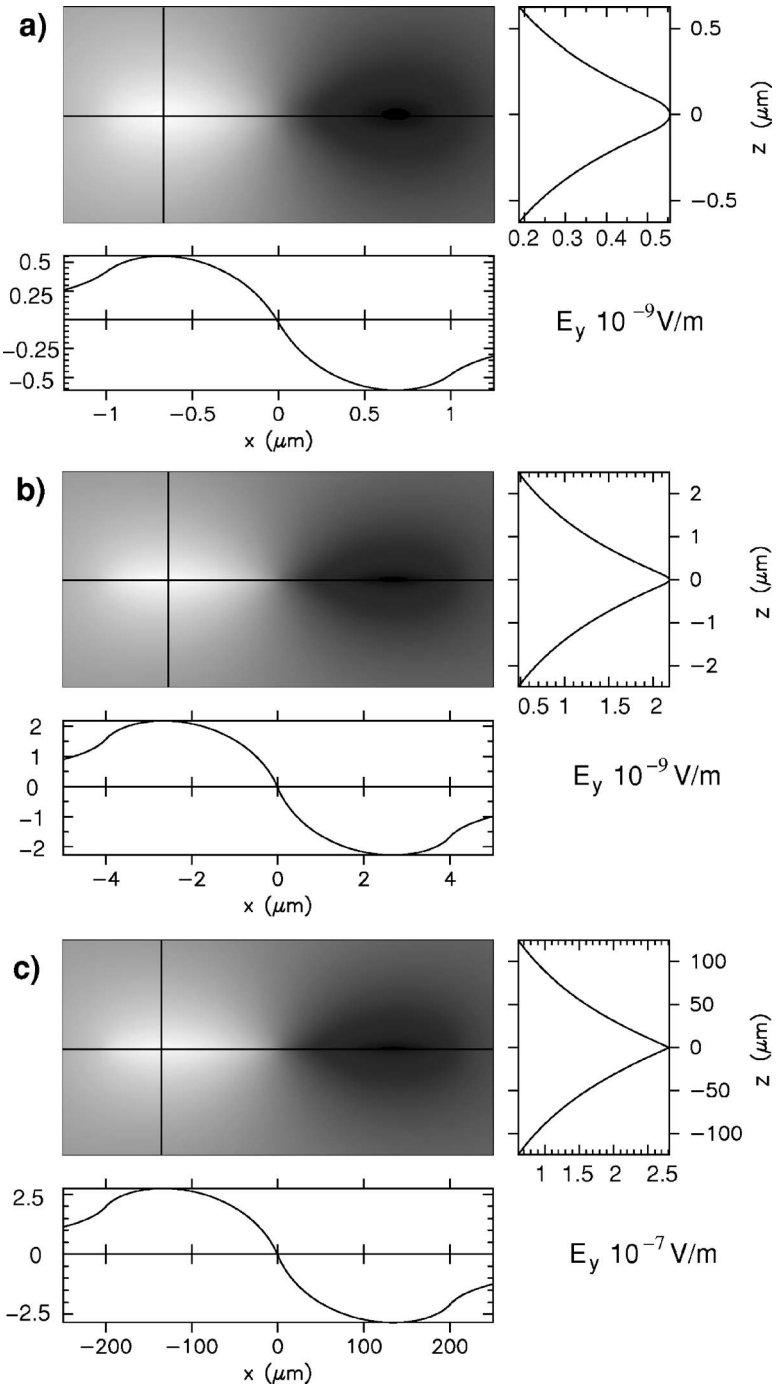

FIG. 6. Distribution of the total inductive electric field $E_{i,y}$ in the (x,z) plane (fully penetrated state) for different widths W of a thin strip. The width of the strip is increased from $W=2$ μm (a), $W=8$ μm, (b) to $W=400$ μm (c). All other parameters are the same as in Figs. 4 and 5.

is rearranged in a way to screen the new flux distribution from the Meissner area. This results in an enhancement of the local current density values in the Meissner area which is induced by the decrease of the current density in the flux-filled regions.

Figure 8 shows the corresponding inductive electric field distribution together with the contributions $E_{i,y}^{(1)}$ and $E_{i,y}^{(2)}$ according to Eqs. (31) and (32). In the flux filled current domains, a similar $E_{i,y}(x)$ pattern is present as in the current domains of a fully penetrated state, with a maximum of $|E_{i,y}(x)|$ which is slightly moved from the sample edge towards the interior of the sample. The electric field in the Meissner area exhibits a sign reversal compared to the adjacent flux-filled current domain with the same current direction. The sign reversal is due to the sign reversal in $\partial_t j_y(x)$ and reflects the increase of the local current density in the Meissner area. Consequently, the electric field is parallel to the current direction in the flux-penetrated regions, whereas it is antiparallel in the area of Meissner currents.

In our own first paper[17] on the determination of electric fields in superconducting films, it was assumed that the electric field in the film is generated only by the moving flux inside the superconductor. The contribution of the temporal change of the magnetic stray field outside the film to the electric field in the film plane was completely disregarded. This approximation considers therefore only the $E_{i,y}^{(1)}$ contri-

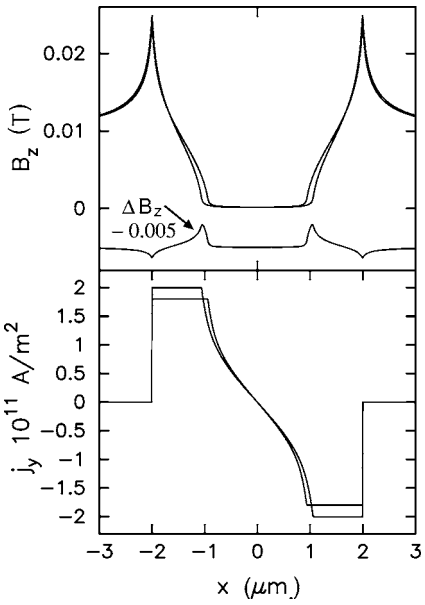

FIG. 7. Calculated temporal change of the normal magnetic flux component $B_z(x)$ of a thin strip in a partly penetrated state. The thickness of the strip is $d=200$ nm, the width $W=4$ μm and $\mu_0 H=10$ mT. The current density in the flux penetrated area is relaxed from $j_c(t_1)=\pm 2\times 10^{11}$ A/m^2 to $j_c(t_2)=\pm 1.8\times 10^{11}$ A/m^2. $\Delta B_z=B_z(t_2)-B_z(t_1)$ denotes the corresponding change of the flux density. For a clearer representation, ΔB_z was shifted by a value of −0.005T.

bution to the total $E_{i,y}$ which is only a minor part. The value of the electric field is underestimated in this article by a factor of $W/(8d)$ which is of the order of 100 for our samples. Consequently, Eq. (3) of Ref. 17 is wrong and should not be used in further work. The application of the correct method to the data in Ref. 17 shows that the obtained local minima and maxima of the electric field at grain boundaries in the bicrystalline YBaCuO films are still present. However, the values and the relative height of the electric field anomalies are not correct.

Other authors[18,29] present electric field distributions for single crystals and slabs, which are based on the one-dimensional case of Eq. (28). The main advantage of using Eq. (30) in this article is that it can be easily extended to the case of two-dimensional current distributions by Fourier transform methods.

V. E_i DISTRIBUTIONS IN 2D FILMS FROM MAGNETO-OPTICAL IMAGING EXPERIMENTS

In this section, we present two-dimensional electric field distributions which are obtained from time resolved magneto-optical imaging experiments. The measurements were done at a square-shaped $YBa_2Cu_3O_{6.95}$ film with 500 nm thickness and a width of 1.2 mm. After zero-field cooling to $T=8$ K, an external magnetic field of $\mu_0 H_{ex}=86$ mT was applied with a ramp rate of 0.3 mT/sec. A series of images of the normal component of the magnetic flux density were taken with a time resolution of 120 msec. The measured light intensities are calibrated into magnetic flux densities as described in Ref. 25.

Figure 9(a) depicts the $B_z(x,y)$ distribution 1.2 sec after application of the external field. The superconducting film is in a partly penetrated state with a Meissner area (dark grey) in the central region. The corresponding current density distribution is shown in Fig. 9(b). One observes a typical Bean-like current density profile with approximately constant critical current density in the flux-filled areas and a Meissner screening current density $j_m \leqslant j_c$ in the flux-free area. Note that the small peaks of the current density at the sample edges are well-known experimental artifacts due to the coupling of in-plane stray fields of the superconductor to the iron garnet indicator.[30,31] This slight error cancels in the time derivative of the current density $\partial_t \mathbf{j}$ which is used for the calculation of $\mathbf{E}_i$ and therefore does not affect the $\mathbf{E}_i(\mathbf{r})$ pattern.

The thermally activated flux creep can be nicely seen in Fig. 10(a), where the temporal change of the flux density $\Delta B_z(x,y)=B_z(x,y,t=1.2\text{ sec})-B_z(x,y,t=0.7\text{ sec})$ is depicted as a grey-scale image. From the time evolution of $B_z(x,y)$, the time evolution of the two-dimensional current density $\mathbf{j}(x,y)$ is obtained by inversion of Biot-Savarts law. According to Eqs. (18) and (19), the in-plane electric field components can be obtained from the time dependence of $\mathbf{j}(x,y)$ in Fourier space. The time evolution of the current density determines the 3D time evolution of the flux distribution in full space outside and inside the sample.

The resulting inductive electric field distribution is visualized in Fig. 10(b). The image shows the absolute value $E_i(x,y)=[E_{i,x}^2(x,y)+E_{i,y}^2(x,y)]^{1/2}$ of the electric field at $t=1.2$ sec after external field sweep. Similarly to the flux domain structure, one observes four domains in the electric field pattern. In each domain, the electric field has a local maximum near the sample edge. The electric field at the current domain boundaries exhibits a local minimum. However, the values remain finite and well above the noise level of our measurement of $E_{noise}\approx 10^{-10}$ V/m. The electric field pattern is similar to the theoretical patterns obtained by Brandt[11] for flux creep in a square-shaped thin film.

Figure 11 depicts the distributions of the electric field components $E_{i,x}(x,y)$ and $E_{i,y}(x,y)$ after fast-Fourier-transform back-transformation of the Fourier coefficients in Eqs. (18) and (19). The electric field distribution in Fig. 11 is characterized by the following features: (i) In the flux-filled domains, the electric field $\mathbf{E}_i$ has the same sign as the current density. Due to opposite current directions, the electric field exhibits a sign reversal in opposite flux domains. (ii) Within an individual flux domain, the electric field is inhomogeneous. $|E_i(x,y)|$ shows a maximum near the middle of each film edge and decays monotoneously from the edges towards the flux front. (iii) As already observed for the calculated data [Figs. 7 and 8] for Meissner regions in thin strips, the electric field displays an additional sign reversal at each flux front, where, however, the direction of the current is unchanged. This sign reversal is related to a different relaxation behavior in the Meissner- and flux-penetrated phases, respectively. Whereas the current density decreases during magnetic relaxation in the flux-penetrated phase, the Meissner

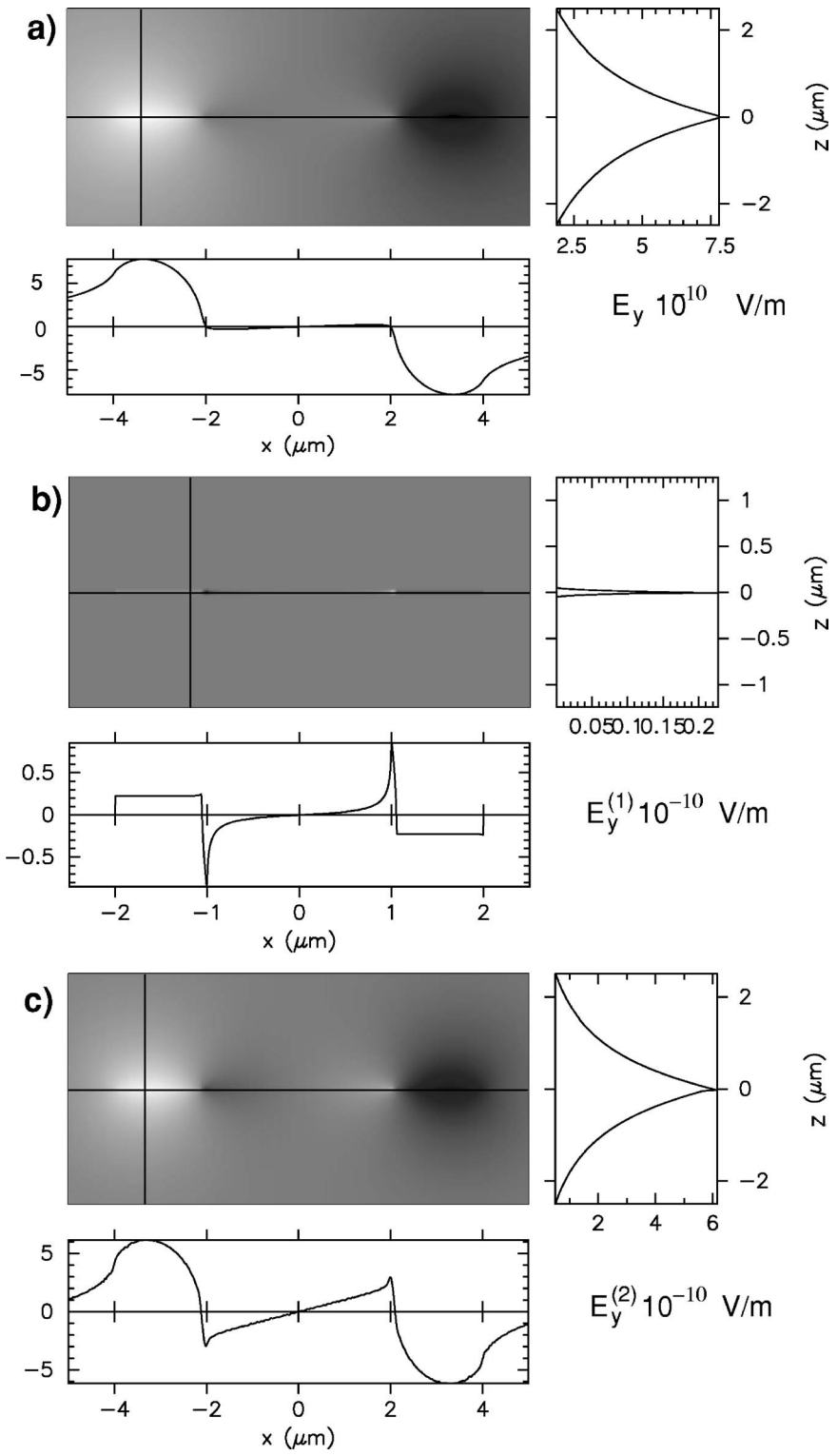

FIG. 8. Electric field distribution in a (x,z) plane of a thin strip due to current relaxation in a partly penetrated state for the same parameters as in Fig. 7. The total inductive electric field $E_{i,y}(x,z)$ [Eq. (28)] is shown in (a), whereas (b) and (c) depict the contributions $E_{i,y}^{(1)}$ and $E_{i,y}^{(2)}$ according to Eqs. (31) and (32), respectively.

screening current locally increases when the flux front moves towards the sample center.

VI. DETERMINATION OF $\mathbf{E}_p$

It is an interesting observation that the determined vector $\mathbf{E}_i(x,y)$ of the local inductive electric field distribution is not parallel to the local current density $\mathbf{j}(x,y)$. We observe systematic deviations between the direction of both vectors. They can be seen, e.g., in Fig. 11, where nonvanishing inductive electric field components $E_{i,x}$ and $E_{i,y}$ are also present in the current domains which are dominated by the j_y and j_x components, respectively (see also Fig. 2 for a comparison with theory). As we will show in this section, the deviation between the inductive in-plane electric field vector $\mathbf{E}_i(x,y)$ and the direction of the current density $\mathbf{j}(x,y)$ can be

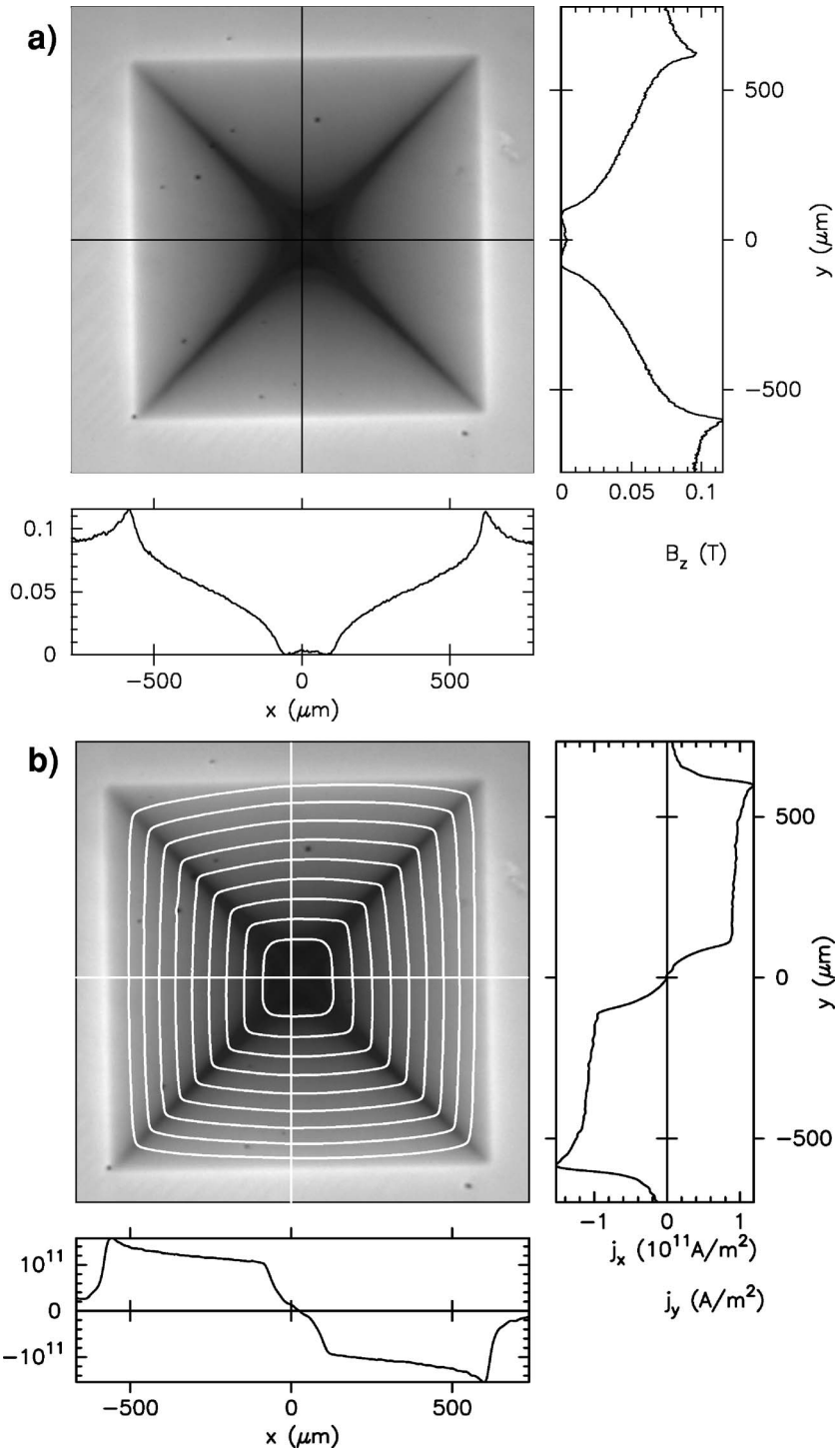

FIG. 9. (a) Calibrated magneto-optical image showing the normal magnetic flux density distribution of a square-shaped YBaCuO film as a grey-scale image. The thin film has a thickness of 500 nm and a width of 1.2 mm. The image is taken 1.2 sec after ramping up the external field from a zero-field-cooled state at $T=8$ K to $\mu_0 H_{ex}=86$ mT. (b) Flux density distribution with superimposed current flow lines and current density profiles for the same state as in (a). The current distribution is obtained by 2D inversion of the Biot-Savart law.

utilized for the determination of the potential contribution $\mathbf{E}_p(x,y)$.

In general, such deviations could have different physical origins, such as a flux-creep Hall effect, where the vortex velocity field is not perpendicular to the current density. Further possible effects are vortex dragging by the superflow, vortex sliding at planar defects, or an anisotropy of the flux-creep resistivity due to the anisotropic orthorhombic crystal structure of the superconductor. However, all these effects can be clearly ruled out because of the following reasons: (i) The observed symmetry of the transverse components of $\mathbf{E}_i$ with two mirror planes Γ_x and Γ_y defined by $x=0$ and $y=0$, respectively, contradicts such effects. (ii) The observed temporal evolution pattern of $B_z(x,y)$ in Fig. 10 clearly shows that the vortex velocity is perpendicular to the direction of $\mathbf{j}(x,y)$. A significant flux-creep Hall effect would be visible in the symmetry breaking of the $\dot{B}_z$ pattern with respect to the Γ_x and Γ_y mirror planes, respectively (Fig. 10). (iii) The orthorhombic crystal structure of the thin films is averaged on length scales below the spatial resolution of our method due to twinning. In addition to the symmetry argument, this

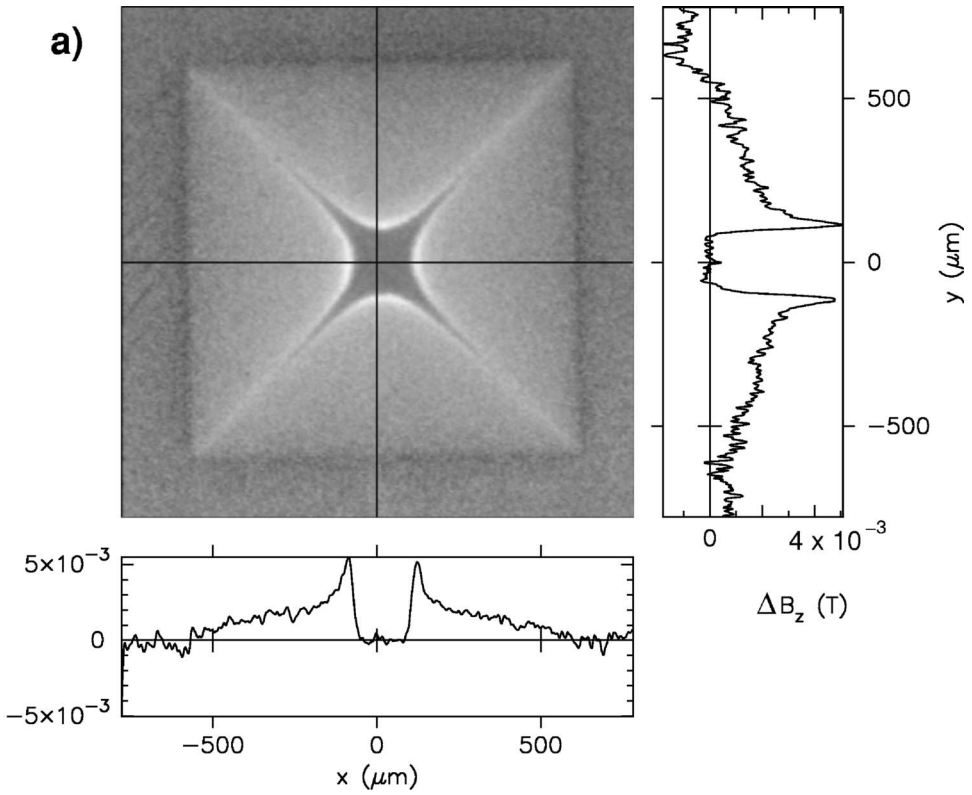

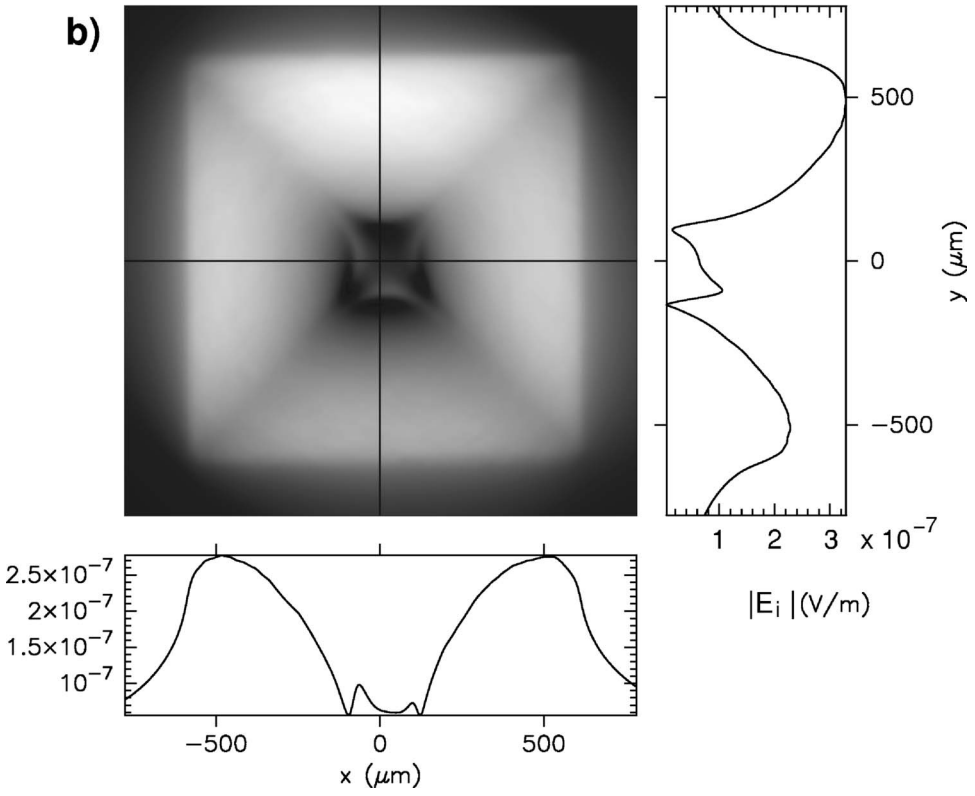

FIG. 10. (a) Time change of the flux density $\Delta B_z(x,y) = B_z(x,y,t=1.2 \text{ sec}) - B_z(x,y,t=0.7 \text{ sec})$ due to thermally activated flux creep. (b) Grey-scale map of the absolute value of inductive electric field distribution in the $z=0$ plane at $t=1.2$ sec of the same state of the sample shown in Fig. 9. The profiles of the electric field are taken along the black lines.

rules out any possible effect due to an in-plane anisotropy of the flux-creep resistivity.

Furthermore, a state with approximatly constant rate of flux creep represents a quasistationary state. Any total $\mathbf{E}$ with a direction deviating from the current direction would give rise to a rearrangement of the current density pattern in that a way to fulfill $\mathbf{E} \| \mathbf{j}$. Consequently, the *total* electric field $\mathbf{E}(x,y)$ must be parallel to $\mathbf{j}(x,y)$ and the vector of the potential electric field must be perpendicular to $\mathbf{j}$, because any $\mathbf{E}_p$ component parallel to $\mathbf{j}$ would change the spatial evolution of the current relaxation and consequently would in fact contribute to $\mathbf{E}_i$.

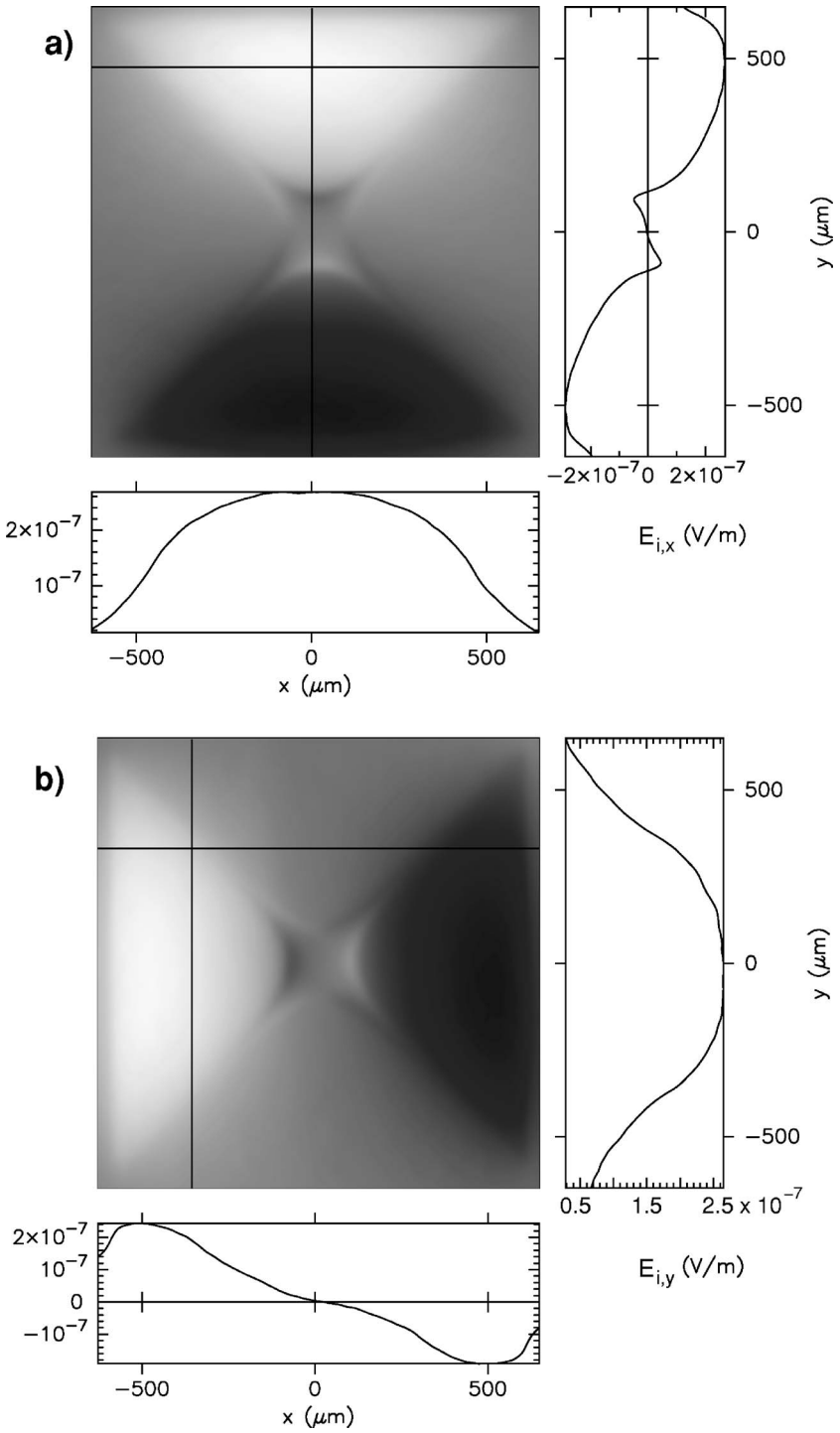

FIG. 11. Grey-scale map of the $E_{i,x}(x,y)$ (a) and $E_{i,y}(x,y)$ (b) components of the inductive electric field in the $z=0$ plane for the same conditions as in Fig. 10.

With θ denoting the deviation angle between $\mathbf{E}_i$ and $\mathbf{j}$, the total electric field is $|\mathbf{E}|=|\mathbf{E}_i|\cos\theta$. The deviation angle can be determined via $\cos\theta=\mathbf{j}\cdot\mathbf{E}_i/(|\mathbf{j}||\mathbf{E}_i|)$, giving, for the total electric field,

$$\mathbf{E}=\frac{\mathbf{j}}{j}|\mathbf{E}_i|\frac{\mathbf{j}\cdot\mathbf{E}_i}{|\mathbf{j}||\mathbf{E}_i|}, \tag{36}$$

with $j=|\mathbf{j}|$. For the in-plane components of the potential electric field $\mathbf{E}_p$ follows

$$E_{p,x}=j_x(\mathbf{E}_i\cdot\mathbf{j})/j^2-E_{i,x},$$

$$E_{p,y}=j_y(\mathbf{E}_i\cdot\mathbf{j})/j^2-E_{i,y}. \tag{37}$$

The resulting potential electric field distributions are depicted in Fig. 12 as grey-scale images. The induced charge density $n_s^{in}=\epsilon_0\nabla\cdot\mathbf{E}_p=-\epsilon_0\nabla\cdot\mathbf{P}$ is depicted in Fig. 13.

The results fully agree with the qualitative theoretical expectations in Fig. 2 which can be directly derived from Faraday's induction law. The potential contribution to the total electric field is generated by a charge density distribution at the current domain boundaries and the sample edges. This charge density is built up by an inhomogeneous sheer creep

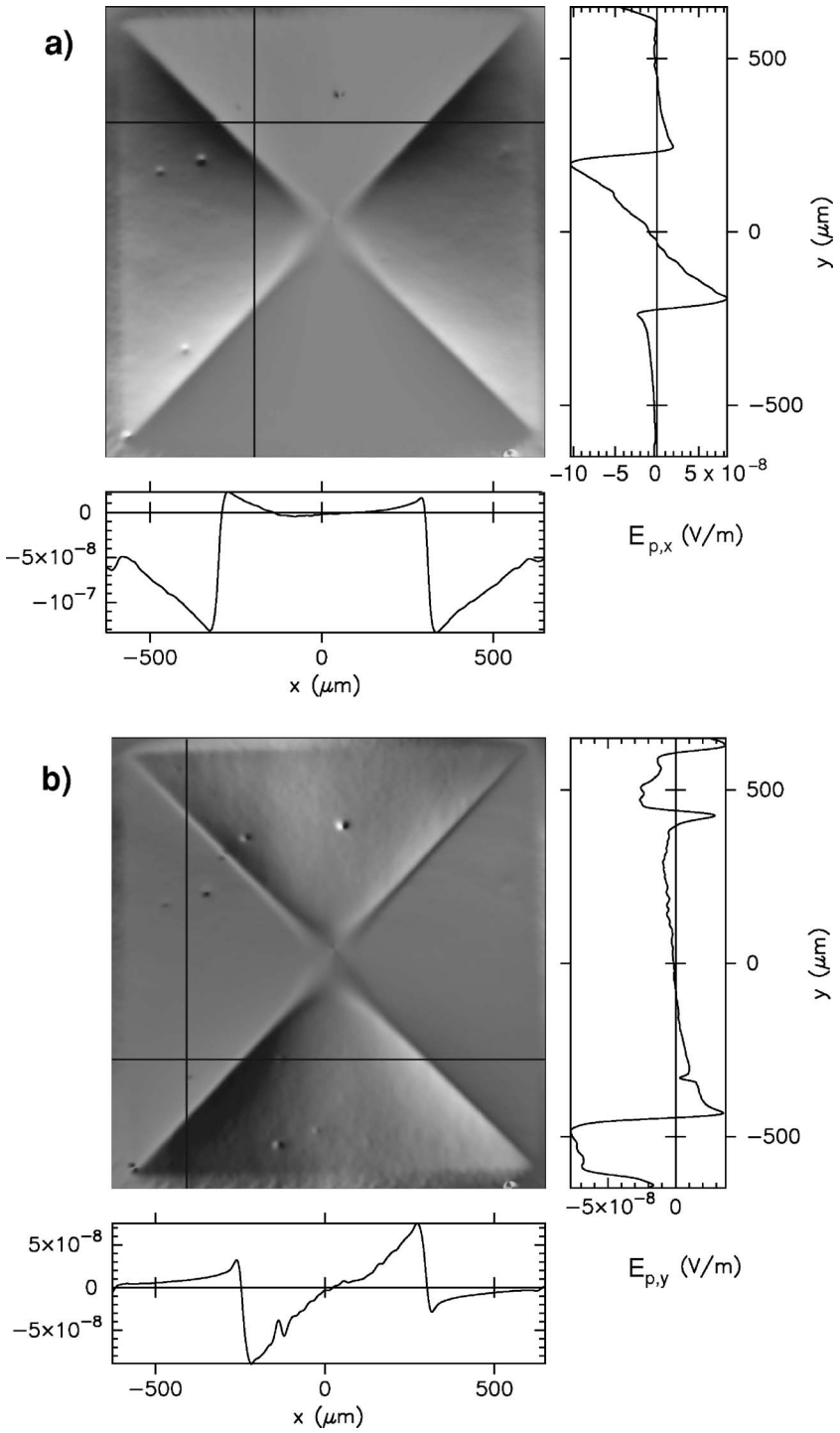

FIG. 12. Grey-scale map of the $E_{p,x}(x,y)$ (a) and $E_{p,y}(x,y)$ (b) components of the potential electric field $\mathbf{E}_p$ in the $z=0$ plane for the same conditions as in Fig. 10. Some small spots in the image are experimental artifacts due to defects in the mirror of the magneto-optical active sensor film.

of vortex columns. The obtained values of the induced charge density of up to 1.4×10^{-14} C/m^3 nicely agree with the order of magnitude estimate which can be obtained from the equation $|n^{in}|=\epsilon_0\partial_t B_{ex}$ for external field sweep in the fully penetrated state in Ref. 11. If we replace the time derivative of the external magnetic field $\partial_t B_{ex}$ by the local quantity $\partial_t B_z \approx (0.1-1)\times10^{-2}$ T/sec (see Fig. 10), we obtain a theoretical order-of-magnitude estimate of $n_s^{in}=(0.8-8)\times10^{-14}$ C/m^3.

The accuracy of the determination of $\mathbf{E}_p$ depends strongly on the accuracy of the determined $\mathbf{j}$ and $\partial_t\mathbf{j}$. Taking all calibration errors of the magneto-optical data into account, the error in $\mathbf{j}$ is smaller than 10% with a comparable error in $\partial_t\mathbf{j}$ (note that some of the errors cancel in the differential images used for the calculation of $\partial_t\mathbf{j}$). Since $\mathbf{E}_p$ depends not only on the absolute values of $\mathbf{E}$ and $\mathbf{j}$ but also on their directions, the error in $\mathbf{P}$ may be larger (up to 30%). There are three minor features in Figs. 12 and 13 which are experimental artifacts and are related to small errors in the calibration of the magneto-optical signals: (i) some small spots in $\mathbf{E}_p$ and n^{in} which are due to defects in the mirror of magneto-optical sensor film [visible also in Fig. 9(a)], (ii) a slight asymmetry

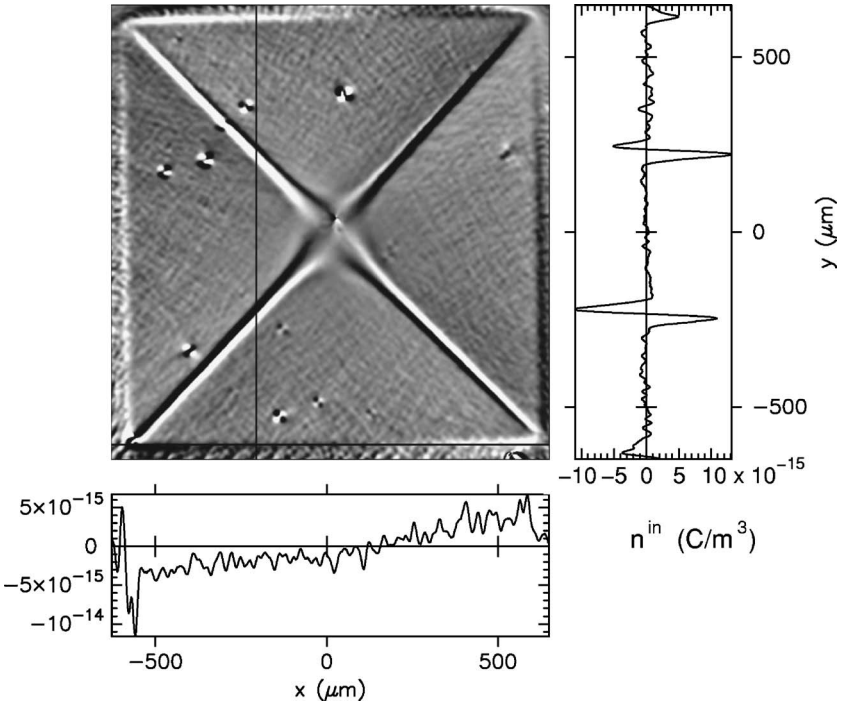

FIG. 13. Grey-scale representation of the induced surface charge density $n_s^{in}=-\epsilon_0\nabla\cdot\mathbf{P}$ for the same conditions as in Fig. 10.

in the P_y pattern in the top j_x domain [Fig. 12(b)] which is related to a small asymmetry in the current stream lines in this area [see Fig. 9(b)], and (iii) whereas the sign change of n_s^{in} at the horizontal sample edges are correct, it is shifted at the vertical sample edges from $y=0$ towards the upper part of the sample. These small artifacts can be clearly identified with small calibration errors in the $B_z(x,y)$ data (due to the small Faraday effect in optical components), and they could be corrected artificially by a linear tilt of the data. The experimental results presented in the article are based on orginal and uncorrected data.

VII. SUMMARY AND CONCLUSIONS

Summarizing the results of this paper, we present a method which allows for the determination of the inductive and potential electric field distributions induced by thermally activated magnetic relaxation in thin-film superconductors of arbitrary shape. The inductive part of $\mathbf{E}_i$ is obtained from the measured time evolution of the normal component of the flux density $B_z(x,y)$.

The observed systematic deviations of the in-plane directions of $\mathbf{E}_i$ from the directions of $\mathbf{j}$ are used for the determination of the $\mathbf{E}_p$ distribution and the induced surface charge density at the sample edges and the current domain boundaries.

We present experimental results for the thermally activated relaxation of a square-shaped YBaCuO thin film after ramping up the external magnetic field. The electric field pattern is very similar to the theoretical expectations of Brandt and Gurevich.[11,12] The determination of the in-plane dielectric polarization field and the induced charge density shows that the sample edges and the current domain boundaries are electrically charged. This charge density seems to play an important role for the shape of the current stream-lines at the current domain boundaries; in particular, its presence is crucial for the strong bending of the supercurrents. The method presented in this article represents a general basis for the analysis of the inductive and potential contributions to the total electric field in samples with complex microstructures such as large defects, current inhomogenities, and grain boundaries.

As a final remark, it is very important to notice that the determination of electric field distributions of superconductors allows to obtain fundamental insights into other dynamic properties of moving vortex ensembles. Having determined the total electric field distribution $\mathbf{E}=\mathbf{E}_i+\mathbf{E}_p$, it is very easy to obtain the dissipated power density $p=\mathbf{j}\cdot\mathbf{E}$, the local flux velocity $\mathbf{v}$ according to $\mathbf{E}=\mathbf{B}\times\mathbf{v}$, and the local activation barrier $U=-k_BT\ln(v/v_0)$, where k_B is the Boltzmann constant, T is the temperature, and v_0 depends only on the material constants of the superconductor. This will allow the space-resolved determination of activation barriers for flux creep which is up to now based on specific models for the $U(j)$ and $U(B)$ relations[32] or restricted to one-dimensional sample geometries.[33]

ACKNOWLEDGMENTS

This work is supported by the Deutsche Forschungsgemeinschaft (DFG). Gratefully acknowledged are helpful discussions with D. Shantsev, E. H. Brandt, M. Indenbom, and C. J. van der Beek.

APPENDIX A

After expressing the inductive electric field by a vector potential $\mathbf{X}(\mathbf{r})$ with

$$\mathbf{E}_i=\nabla\times\mathbf{X}, \tag{A1}$$

one obtains

$$\nabla \times \mathbf{E}_i = \nabla \cdot (\nabla \cdot \mathbf{X}) - \Delta \mathbf{X} = -\dot{\mathbf{B}}. \tag{A2}$$

Without loss of general validity, the gauge $\nabla \cdot \mathbf{X} = 0$ can be applied and Eq. (A2) can be integrated by means of the Green function of the Laplace operator, giving

$$\mathbf{X} = \frac{1}{4\pi} \int d^3r' \frac{\dot{\mathbf{B}}(\mathbf{r}')}{|\mathbf{r} - \mathbf{r}'|}. \tag{A3}$$

For the inductive electric field, we find

$$\mathbf{E}_i = \frac{1}{4\pi} \nabla \times \int \frac{\dot{\mathbf{B}}}{|\mathbf{r} - \mathbf{r}'|} d^3r', \tag{A4}$$

yielding directly Eq. (7).

APPENDIX B

For the $E_{i,x}$, $E_{i,y}$, and $E_{i,z}$ components of the inductive electric field, we obtain, from Eq. (7),

$$E_{i,x}(\mathbf{r}) = \int d^3r' G(\mathbf{r} - \mathbf{r}') \dot{B}_y(\mathbf{r}') - \int d^3r' L(\mathbf{r} - \mathbf{r}') \dot{B}_z(\mathbf{r}'), \tag{B1}$$

$$E_{i,y}(\mathbf{r}) = \int d^3r' H(\mathbf{r} - \mathbf{r}') \dot{B}_z(\mathbf{r}') - \int d^3r' G(\mathbf{r} - \mathbf{r}') \dot{B}_x(\mathbf{r}'), \tag{B2}$$

and

$$E_{i,z}(\mathbf{r}) = \int d^3r' L(\mathbf{r} - \mathbf{r}') \dot{B}_x(\mathbf{r}') - \int d^3r' H(\mathbf{r} - \mathbf{r}') \dot{B}_y(\mathbf{r}'), \tag{B3}$$

with the integral kernels

$$G = \frac{1}{4\pi} \frac{z - z'}{|\mathbf{r} - \mathbf{r}'|^3}, \tag{B4}$$

$$H = \frac{1}{4\pi} \frac{x - x'}{|\mathbf{r} - \mathbf{r}'|^3}, \tag{B5}$$

and

$$L = \frac{1}{4\pi} \frac{y - y'}{|\mathbf{r} - \mathbf{r}'|^3}. \tag{B6}$$

Applying two-dimensional Fourier transforms in the (x,y) plane, one obtains, for the Fourier-transformed kernels,

$$g = \frac{1}{2} \operatorname{sgn}(z - z') e^{-k|z - z'|}, \tag{B7}$$

$$h = \frac{i}{2} \frac{k_x}{k} e^{-k|z - z'|}, \tag{B8}$$

and

$$l = \frac{i}{2} \frac{k_y}{k} e^{-k|z - z'|}, \tag{B9}$$

with wave number $k = \sqrt{k_x^2 + k_y^2}$.

The Fourier coefficients of $E_{i,x}$ can be expressed as

$$\tilde{E}_{i,x}(k_x,k_y,z) = \tilde{E}_{i,x}^{(1)} + \tilde{E}_{i,x}^{(2)} = \int_{-\infty}^{\infty} dz' g(k_x,k_y,z,z') \tilde{\dot{B}}_y(k_x,k_y,z') - \int_{-\infty}^{\infty} dz' l(k_x,k_y,z,z') \tilde{\dot{B}}_z(k_x,k_y,z'). \tag{B10}$$

Similarly, the Fourier coefficients of $E_{i,y}$ are given by

$$\tilde{E}_{i,y}(k_x,k_y,z) = \tilde{E}_{i,y}^{(1)} + \tilde{E}_{i,y}^{(2)} = \int_{-\infty}^{\infty} dz' h(k_x,k_y,z,z') \tilde{\dot{B}}_z(k_x,k_y,z') - \int_{-\infty}^{\infty} dz' g(k_x,k_y,z,z') \tilde{\dot{B}}_x(k_x,k_y,z') \tag{B11}$$

and those of $E_{i,z}$ are written

$$\tilde{E}_{i,z}(k_x,k_y,z) = \tilde{E}_{i,z}^{(1)} + \tilde{E}_{i,z}^{(2)} = \int_{-\infty}^{\infty} dz' l(k_x,k_y,z,z') \tilde{\dot{B}}_x(k_x,k_y,z') - \int_{-\infty}^{\infty} dz' h(k_x,k_y,z,z') \tilde{\dot{B}}_y(k_x,k_y,z'). \tag{B12}$$

APPENDIX C

Once the time evolution of the two-dimensional current density in the film is known, the time evolution of $\mathbf{B}(\mathbf{r},t)$ in the entire space inside and outside the superconducting film can be determined by the Biot-Savart law:

$$\mathbf{B}(\mathbf{r},t) = \frac{\mu_0}{4\pi} \int \frac{\mathbf{j}(\mathbf{r}',t) \times (\mathbf{r} - \mathbf{r}')}{|\mathbf{r} - \mathbf{r}'|} d^3r'. \tag{C1}$$

After two-dimensional Fourier transforms, we can again use the Fourier-transformed integral kernels g, h, and l. We obtain, for the Fourier coefficients of the B_z component,

$$\tilde{B}_z(k_x,k_y,z) = \frac{i\mu_0}{2} \int_{-d/2}^{d/2} dz' e^{-k|z - z'|} \alpha, \tag{C2}$$

with

$$\alpha = \frac{k_y}{k} \tilde{j}_x(k_x,k_y,z') - \frac{k_x}{k} \tilde{j}_y(k_x,k_y,z'). \tag{C3}$$

Assuming that the current density does not vary in the z direction within the film thickness $|z| \leqslant d/2$, this yields

$$\tilde{B}_z(k_x,k_y,z) = \frac{i\mu_0}{2} \alpha \begin{cases} \frac{2}{k} e^{-k|z|} \sinh\left(\frac{kd}{2}\right), & |z| \geqslant \frac{d}{2}, \\ \frac{1}{k}(2 - e^{-k(z+d/2)} - e^{k(z-d/2)}), & |z| < \frac{d}{2}. \end{cases} \tag{C4}$$

Similarly, the B_x and B_y components are given after two-dimensional Fourier transforms by

$$\tilde{B}_x(k_x,k_y,z) = \mu_0 \int_{-d/2}^{d/2} dz' \tilde{j}_y g \tag{C5}$$

and

$$\tilde{B}_y(k_x,k_y,z) = -\mu_0 \int_{-d/2}^{d/2} dz' \tilde{j}_x g, \tag{C6}$$

yielding

$$\tilde{B}_x(k_x,k_y,z) = \frac{\mu_0 \tilde{j}_y}{2k}\{e^{-k|z-d/2|} - e^{-k|z+d/2|}\} \tag{C7}$$

and

$$\tilde{B}_y(k_x,k_y,z) = -\frac{\mu_0 \tilde{j}_x}{2k}\{e^{-k|z-d/2|} - e^{-k|z+d/2|}\}. \tag{C8}$$

APPENDIX D

We calculate the two contributions to the Fourier coefficients of $E_{i,x}$ in Eq. (9). For the first contribution one obtains

$$\begin{aligned}\tilde{E}^{(1)}_{i,x}(k_x,k_y,z) &= \int_{-\infty}^{\infty} dz' g(k_x,k_y,z,z')\dot{\tilde{B}}_y(k_x,k_y,z') \\ &= \frac{\mu_0}{4k}\partial_t \tilde{j}_x(k_x,k_y)\int_{-\infty}^{\infty} dz' \mathrm{sgn}(z-z')e^{-k|z-z'|} \\ &\quad \times \{e^{-k|z'+d/2|} - e^{-k|z'-d/2|}\}. \end{aligned} \tag{D1}$$

At the $z=0$ plane, the integral gives

$$\frac{1}{k}\{e^{-kd/2}(dk+1) - e^{kd/2}\}, \tag{D2}$$

and in the approximation $kd \leqslant 1$ the first-order approximation $e^{kd/2} \approx 1 + kd/2$ gives for the integral

$$-\frac{1}{2}kd^2. \tag{D3}$$

The second contribution in Eq. (9) is given by

$$\begin{aligned}\tilde{E}^{(2)}_{i,x}(k_x,k_y,z) &= -\int_{-\infty}^{\infty} dz' l(k_x,k_y,z,z')\dot{\tilde{B}}_z(k_x,k_y,z') \\ &= -\frac{\mu_0}{4}\frac{k_y}{k^2}\dot{\alpha}\{f_1 + f_2 + f_3\}, \end{aligned} \tag{D4}$$

with

$$f_1 = \int_{-\infty}^{-d/2} dz' 2e^{-k|z-z'|}e^{-k|z'|}\sinh\left(\frac{kd}{2}\right),$$

$$f_2 = \int_{d/2}^{\infty} dz' 2e^{-k|z-z'|}e^{-k|z'|}\sinh\left(\frac{kd}{2}\right),$$

$$f_3 = \int_{-d/2}^{d/2} dz' e^{-k|z-z'|}\{2 - e^{-k(z'+d/2} - e^{k(z'-d/2}\}, \tag{D5}$$

and

$$\dot{\alpha} = \frac{k_y}{k}\partial_t \tilde{j}_x(k_x,k_y,z') - \frac{k_x}{k}\partial_t \tilde{j}_y(k_x,k_y,z'). \tag{D6}$$

At the $z=0$ plane, the functions f_i can be evaluated analytically:

$$f_1 = f_2 = \frac{1}{k}\sinh\left(\frac{kd}{2}\right)e^{-kd},$$

$$f_3 = -\frac{1}{k}\{5e^{kd} + dke^{kd} - 1 - 4e^{3/2kd}\}e^{-3/2kd}. \tag{D7}$$

For $kd \leqslant 1$ and using the first-order approximation $e^{kd/2} \approx 1 + kd/2$ one obtains

$$\tilde{E}^{(2)}_{i,x}(k_x,k_y,z=0) = \frac{\mu_0}{2k}\frac{k_y}{k^2}\sinh\left(\frac{kd}{2}\right)\dot{\alpha}. \tag{D8}$$

[1] J. Bardeen and M. J. Stephen, Phys. Rev. A **140**, 1197 (1965).
[2] P. Nozières and W. F. Vinen, Philos. Mag. **14**, 667 (1966).
[3] S. Hofmann and R. Kümmel, Phys. Rev. B **57**, 7904 (1998).
[4] Y. Yeshurun, A. P. Malozemoff, and A. Shaulov, Rev. Mod. Phys. **68**, 911 (1996).
[5] W. Henderson, E. Y. Andrei, and M. J. Higgins, Phys. Rev. Lett. **81**, 2352 (1998).
[6] M. V. Feigelman, V. B. Geshkenbein, A. I. Larkin, and V. I. Vinokur, Phys. Rev. Lett. **63**, 2303 (1989).
[7] T. Matsuda, K. Harada, H. Kasai, O. Kamimura, and A. Tonomura, Science **271**, 1393 (1996).
[8] C. J. Olson, C. Reichhardt, and F. Nori, Phys. Rev. B **56**, 6175 (1997).
[9] R. Prozorov and D. Giller, Phys. Rev. B **59**, 14687 (1999).
[10] T. H. Johansen, M. Baziljevich, D. V. Shantsev, P. E. Goa, Y. M. Galperin, W. N. Kang, H. J. Kim, E. M. Choi, M. S. Kim, and S. I. Lee, Europhys. Lett. **59**, 599 (2002).
[11] E. H. Brandt, Phys. Rev. B **52**, 15442 (1995).
[12] A. Gurevich and E. H. Brandt, Phys. Rev. Lett. **73**, 178 (1994).
[13] E. H. Brandt, Phys. Rev. Lett. **76**, 4030 (1996).
[14] A. Gurevich and J. McDonald, Phys. Rev. Lett. **81**, 2546 (1998).
[15] A. Gurevich and M. Friesen, Phys. Rev. B **62**, 4004 (2000).
[16] E. H. Brandt, Rep. Prog. Phys. **58**, 1465 (1995).
[17] Ch. Jooss, K. Guth, V. Born, and J. Albrecht, Phys. Rev. B **65**, 014505 (2001).
[18] D. Giller, Y. Abulafia, R. Prozorov, Y. Wolfus, A. Shaulov, and Y. Yeshurun, Phys. Rev. B **57**, R14080 (1998).
[19] P. Lipavsky, J. Kolacek, J. J. Mares, and K. Morawetz, Phys. Rev. B **65**, 012507 (2001).
[20] P. Lipavsky, J. Kolacek, K. Morawetz, and E. H. Brandt, Phys. Rev. B **65**, 144511 (2002).
[21] Ch. Jooss, A. Forkl, R. Warthmann, and H. Kronmüller, Physica C **299**, 215 (1998).
[22] F. London and H. London, Proc. R. Soc. London, Ser. A **149**, 71 (1935).
[23] M. W. Coffey and Z. Hao, Phys. Rev. B **44**, 5230 (1991).

[24] Y. Matsuda and K. Kumagai, in *Vortices in Unconventional Superconductors and Superfluids*, edited by R. P. Huebener, N. Schopohl, and G. E. Volovik (Springer, Berlin, 2002), p. 283.
[25] Ch. Jooss, J. Albrecht, H. Kuhn, S. Leonhardt, and H. Kronmüller, Rep. Prog. Phys. **65**, 651 (2002).
[26] E. H. Brandt, M. V. Indenbom, and A. Forkl, Europhys. Lett. **22**, 735 (1993).
[27] Ch. Jooss, A. Forkl, R. Warthmann, H.-U. Habermeier, B. Leibold, and H. Kronmüller, Physica C **266**, 235 (1996).
[28] Th. Schuster, H. Kuhn, and E. H. Brandt, Phys. Rev. B **51**, 697 (1995).
[29] D. V. Shantsev, Y. M. Galperin, and T. H. Johansen, Phys. Rev. B **65**, 184512 (2002).
[30] T. H. Johansen, M. Baziljevich, H. Bratsberg, Y. Galperin, P. E. Lindelof, Y. Shen, and P. Vase, Phys. Rev. B **54**, 16264 (1996).
[31] F. Laviano, D. Botta, A. Chiodoni, R. Gerbaldo, G. Ghigo, L. Gozzelino, and E. Mezzetti, Phys. Rev. B **68**, 014507 (2003).
[32] R. Warthmann, J. Albrecht, H. Kronmüller, and Ch. Jooss, Phys. Rev. B **62**, 15226 (2000).
[33] Y. Abulafia, A. Shaulov, Y. Wolfus, R. Prozorov, L. Burlachkov, Y. Yeshurun, D. Majer, E. Zeldov, and V. M. Vinokur, Phys. Rev. Lett. **75**, 2404 (1995).